

Global inventory and characterization of pyroclastic deposits on Mercury: New insights into pyroclastic activity from MESSENGER orbital data

Timothy A. Goudge, James W. Head, Laura Kerber, David T. Blewett, Brett W. Denevi, Deborah L. Domingue, Jeffrey J. Gillis-Davis, Klaus Gwinner, Jörn Helbert, Gregory M. Holsclaw, et al.

▶ **To cite this version:**

Timothy A. Goudge, James W. Head, Laura Kerber, David T. Blewett, Brett W. Denevi, et al.. Global inventory and characterization of pyroclastic deposits on Mercury: New insights into pyroclastic activity from MESSENGER orbital data. Journal of Geophysical Research. Planets, 2014, 119 (3), pp.635-658. 10.1002/2013JE004480 . hal-01083738

HAL Id: hal-01083738

https://polytechnique.hal.science/hal-01083738

Submitted on 3 Jan 2022

HAL is a multi-disciplinary open access archive for the deposit and dissemination of scientific research documents, whether they are published or not. The documents may come from teaching and research institutions in France or abroad, or from public or private research centers.

L'archive ouverte pluridisciplinaire **HAL**, est destinée au dépôt et à la diffusion de documents scientifiques de niveau recherche, publiés ou non, émanant des établissements d'enseignement et de recherche français ou étrangers, des laboratoires publics ou privés.

Copyright

AGU PUBLICATIONS

JGR

Journal of Geophysical Research: Planets

RESEARCH ARTICLE
10.1002/2013JE004480

Key Points:
- We expand the catalog of pyroclastic deposits on Mercury from 40 to 51
- Stratigraphic relationships suggest emplacement over a prolonged interval
- Deposits exhibit distinct spectral signatures with interdeposit variability

Correspondence to:
T. A. Goudge,
Tim_Goudge@brown.edu

Citation:
Goudge, T. A., et al. (2014), Global inventory and characterization of pyroclastic deposits on Mercury: New insights into pyroclastic activity from MESSENGER orbital data, *J. Geophys. Res. Planets*, *119*, 635–658, doi:10.1002/2013JE004480.

Received 4 JUL 2013
Accepted 5 FEB 2014
Accepted article online 12 FEB 2014
Published online 28 MAR 2014

Global inventory and characterization of pyroclastic deposits on Mercury: New insights into pyroclastic activity from MESSENGER orbital data

Timothy A. Goudge[1], James W. Head[1], Laura Kerber[2], David T. Blewett[3], Brett W. Denevi[3], Deborah L. Domingue[4], Jeffrey J. Gillis-Davis[5], Klaus Gwinner[6], Jörn Helbert[6], Gregory M. Holsclaw[7], Noam R. Izenberg[3], Rachel L. Klima[3], William E. McClintock[7], Scott L. Murchie[3], Gregory A. Neumann[8], David E. Smith[9], Robert G. Strom[10], Zhiyong Xiao[10,11], Maria T. Zuber[9], and Sean C. Solomon[12,13]

[1]Department of Geological Sciences, Brown University, Providence, Rhode Island, USA, [2]Laboratoire de Météorologie Dynamique, Centre National de la Recherche Scientifique, Université Pierre et Marie Curie, Institut Pierre-Simon Laplace, Paris, France, [3]The Johns Hopkins University Applied Physics Laboratory, Laurel, Maryland, USA, [4]Planetary Science Institute, Tucson, Arizona, USA, [5]Hawai'i Institute of Geophysics and Planetology, University of Hawai'i at Mānoa, Honolulu, Hawaii, USA, [6]Institute of Planetary Research, Deutsches Zentrum für Luft- und Raumfahrt, Berlin, Germany, [7]Laboratory for Atmospheric and Space Physics, University of Colorado Boulder, Boulder, Colorado, USA, [8]Solar System Exploration Division, NASA Goddard Space Flight Center, Greenbelt, Maryland, USA, [9]Department of Earth, Atmospheric and Planetary Sciences, Massachusetts Institute of Technology, Cambridge, Massachusetts, USA, [10]Lunar and Planetary Laboratory, University of Arizona, Tucson, Arizona, USA, [11]Planetary Science Institute, China University of Geosciences, Wuhan, China, [12]Department of Terrestrial Magnetism, Carnegie Institution of Washington, Washington, District of Columbia, USA, [13]Lamont-Doherty Earth Observatory, Columbia University, Palisades, New York, USA

Abstract We present new observations of pyroclastic deposits on the surface of Mercury from data acquired during the orbital phase of the MErcury Surface, Space ENvironment, GEochemistry, and Ranging (MESSENGER) mission. The global analysis of pyroclastic deposits brings the total number of such identified features from 40 to 51. Some 90% of pyroclastic deposits are found within impact craters. The locations of most pyroclastic deposits appear to be unrelated to regional smooth plains deposits, except some deposits cluster around the margins of smooth plains, similar to the relation between many lunar pyroclastic deposits and lunar maria. A survey of the degradation state of the impact craters that host pyroclastic deposits suggests that pyroclastic activity occurred on Mercury over a prolonged interval. Measurements of surface reflectance by MESSENGER indicate that the pyroclastic deposits are spectrally distinct from their surrounding terrain, with higher reflectance values, redder (i.e., steeper) spectral slopes, and a downturn at wavelengths shorter than ~400 nm (i.e., in the near-ultraviolet region of the spectrum). Three possible causes for these distinctive characteristics include differences in transition metal content, physical properties (e.g., grain size), or degree of space weathering from average surface material on Mercury. The strength of the near-ultraviolet downturn varies among spectra of pyroclastic deposits and is correlated with reflectance at visible wavelengths. We suggest that this interdeposit variability in reflectance spectra is the result of either variable amounts of mixing of the pyroclastic deposits with underlying material or inherent differences in chemical and physical properties among pyroclastic deposits.

1. Introduction

Multispectral images of Mercury acquired during three flybys by the MErcury Surface, Space ENvironment, GEochemistry, and Ranging (MESSENGER) spacecraft [*Solomon et al.*, 2008] revealed a number of sites on the surface that were identified as pyroclastic deposits formed through explosive volcanic processes [*Head et al.*, 2008, 2009; *Murchie et al.*, 2008; *Robinson et al.*, 2008; *Blewett et al.*, 2009; *Kerber et al.*, 2009, 2011]. These sites are all characterized by high-reflectance deposits with diffuse borders that are approximately centered on irregularly shaped, rimless pits. The deposits have a "red" spectral slope (i.e., reflectance increases with increasing wavelength) [*Blewett et al.*, 2009; *Kerber et al.*, 2009, 2011]. The central pits are interpreted to be the source vents for the pyroclastic deposits [*Kerber et al.*, 2011].

©2014. American Geophysical Union. All Rights Reserved.

These pyroclastic deposits provide insight into the abundances, composition, and distribution of volatiles in Mercury's interior [*Kerber et al*., 2009; *Zolotov*, 2011]. Moreover, their presence constitutes an important constraint on the formation of the inner solar system, because Mercury's crust and mantle are not as volatile depleted as predicted by most earlier formation models for the innermost planet [*Cameron*, 1985; *Benz et al*., 1988; *Boynton et al*., 2007; *Solomon et al*., 2007; *Kerber et al*., 2009, 2011]. The possibility of explosive volcanism on Mercury had been suggested on the basis of analysis of Mariner 10 images [e.g., *Rava and Hapke*, 1987; *Robinson and Lucey*, 1997], but the large number of deposits identified from flyby images [*Kerber et al*., 2011] was surprising, and the distribution and geological setting of these deposits yielded new and important clues to Mercury's complex geologic evolution.

From Mercury Dual Imaging System (MDIS) [*Hawkins et al*., 2007] images acquired during MESSENGER's three flybys of Mercury, *Kerber et al*. [2011] compiled a catalog of 40 pyroclastic deposits. The deposits are primarily located on the floors of impact craters and along the rim of the Caloris impact basin [*Kerber et al*., 2011]. Deposits were identified by high-reflectance, spectrally red terrain surrounding irregularly shaped, rimless pits. The radial extent of 35 of the 40 deposits was found to range from ~7 to 71 km [*Kerber et al*., 2011]. Together with a ballistic trajectory model, these radial extents were used to estimate the volatile content needed to emplace pyroclastic material to these distances from the source vent. Calculations indicated volatile contents of ~1600–16,000 ppm CO (or an equivalent amount of other volatile species) [*Kerber et al*., 2011], figures far larger than those previously hypothesized for Mercury's interior [e.g., *Boynton et al*., 2007; *Kerber et al*., 2011]. *Kerber et al*. [2011] also used MDIS color images to show that none of the identified pyroclastic deposits displays a 1000 nm absorption feature in its reflectance spectrum that would be indicative of a crystal field effect produced by octahedrally coordinated Fe^{2+} bound in the structure of silicate minerals [*Burns*, 1993a].

Although MESSENGER flyby data were sufficient to recognize many of the pyroclastic deposits on Mercury [*Head et al*., 2008, 2009; *Murchie et al*., 2008; *Robinson et al*., 2008; *Blewett et al*., 2009; *Kerber et al*., 2009, 2011], the insertion of the MESSENGER spacecraft into orbit about Mercury on 18 March 2011 has provided images at higher spatial resolution and with more complete spatial coverage than were available during the three flybys, as well as such additional global data sets as spectral reflectance and topography. In this paper, we use orbital observations to augment the earlier catalog of pyroclastic deposits developed by *Kerber et al*. [2011] and to characterize those deposits in greater detail. Specific goals of this analysis are (1) to determine the morphometry of the vents associated with the pyroclastic deposits, (2) to assess whether these deposits tend to occur in specific settings or in association with specific geologic units, (3) to estimate the relative age of these deposits and their associated pyroclastic activity, and (4) to further our understanding of the spectral characteristics of the pyroclastic deposits.

2. Data Sets Used

To address the goals of this study, we used three data sets from instruments on the MESSENGER spacecraft. The distribution and the morphometry of the deposits and associated vents were investigated with narrow-angle camera (NAC) and wide-angle camera (WAC) images obtained with MDIS. The spatial resolution of the utilized images ranged from ~15 to 200 m/pixel for the NAC and ~60 to 500 m/pixel for the WAC. Because of MESSENGER's highly eccentric orbit and high northern periapsis [*Solomon et al*., 2007], the spatial resolution of MDIS NAC and WAC images depend on latitude; images at high northern latitudes have markedly higher spatial resolution than images of the southern hemisphere. However, a global campaign of mapping the surface of Mercury at ~250 m/pixel with MDIS has been completed, and the global MDIS NAC- and WAC-derived mosaic at ~250 m/pixel was also utilized in this study when no images of higher resolution were available. Analyzed MDIS NAC, WAC, and mosaic images were geographically referenced using the U.S. Geological Survey's Integrated Software for Imagers and Spectrometers. These data were then analyzed in Environmental Systems Research Institute's ArcMap geographic information system software, which allows for coregistration of an array of data sets.

Vent depths were determined from topographic profiles obtained with the Mercury Laser Altimeter (MLA) instrument [*Cavanaugh et al*., 2007]. The MLA instrument measures the range from the MESSENGER spacecraft to a point on the surface of Mercury, with a footprint diameter of ~15–100 m and an along-track spacing of ~400 m [*Cavanaugh et al*., 2007; *Zuber et al*., 2012]. The topographic datum for analyzed MLA data

©2014. American Geophysical Union. All Rights Reserved.

is a sphere of radius 2440 km. MLA has a range precision (i.e., shot-to-shot vertical precision) of $<$1 m under nadir-viewing conditions, and the accuracy of the topography with respect to Mercury's center of mass is $<$20 m [*Cavanaugh et al*., 2007; *Zuber et al*., 2012].

Individual MLA measurements of elevation were analyzed alongside coregistered MDIS images to obtain topographic information for the pyroclastic source vents. Although MLA profile measurements have been interpolated to produce gridded topographic data sets, the resolution of the gridded dada is insufficient for measuring features of small areal extent. Whereas the along-track spacing of MLA footprints remains relatively constant at ~400 m [*Cavanaugh et al*., 2007; *Zuber et al*., 2012], the track-to-track spacing increases with increasing distance from MESSENGER's periapsis latitude, and there is little southern hemisphere coverage by MLA because the spacecraft altitude is too high for laser ranging [*Cavanaugh et al*., 2007; *Solomon et al*., 2007]. Available MLA profiles across individual pyroclastic source vents are therefore sparse at this time.

The spectral reflectance of pyroclastic deposits was investigated with two data sets. MDIS WAC eight-filter color images were used to assess the general spectral signature of the pyroclastic deposits. Although the MDIS WAC camera has 11 color filters, with band centers ranging from ~430 to 1010 nm [*Hawkins et al*., 2007], the mapping phase of MESSENGER's primary orbital mission concentrated on the acquisition of a global mosaic of eight-filter color images, obtained with band pass filters that have wavelength centers at ~430, 480, 560, 630, 750, 830, 900, and 1000 nm [*Hawkins et al*., 2007]. All analyzed MDIS color images were photometrically corrected using the Hapke model of *Domingue et al*. [2010, 2011], which normalizes the data to an incidence angle of 30°, an emission angle of 0°, and a phase angle of 30°. The high spatial resolution of MDIS color images provides an excellent basis for locating and identifying the boundaries of pyroclastic deposits [e.g., *Blewett et al*., 2009; *Kerber et al*., 2009, 2011], but the low spectral resolution is not as favorable for detailed spectral characterization.

To perform such analyses, higher spectral resolution data from the Visible and Infrared Spectrograph (VIRS) portion of the Mercury Atmospheric and Surface Composition Spectrometer (MASCS) instrument [*McClintock and Lankton*, 2007] were analyzed. VIRS is a point spectrometer with a 0.023° field of view that collects reflectance data from the surface of Mercury across the wavelength range ~300–1450 nm at a spectral resolution of ~5 nm [*McClintock and Lankton*, 2007]. VIRS has two spectral channels, one in the ultraviolet (UV) to visible (VIS) region from ~300 to 1050 nm, and one in the near-infrared (NIR) region from ~850 to 1450 nm. Because the NIR channel of the VIRS instrument is susceptible to noise at the elevated temperatures experienced on Mercury's dayside, however, only data from the UV–VIS channel of the VIRS instrument were analyzed here. The analyzed MASCS data were converted to reflectance using the techniques described in detail by *Holsclaw et al*. [2010], and a first-order photometric correction was applied as described by *Izenberg et al*. [2014], which normalizes the MASCS data to incidence and emission angles of 45° and a phase angle of 90°.

3. Update to the Global Catalog of Pyroclastic Deposits

To build on the global catalog of pyroclastic deposits presented by *Kerber et al*. [2011], we examined MDIS NAC and WAC images from the first 10 months of MESSENGER's orbital mission phase to seek evidence for rimless depressions that could be source vents for pyroclastic deposits [*Kerber et al*., 2009, 2011]. Identified candidate pyroclastic vents were studied with individual MDIS WAC eight-filter color images to determine their spectral signature.

In order to be added to the global catalog of pyroclastic deposits, newly identified candidate vents had to exhibit two distinct spectral characteristics associated with pyroclastic deposits previously identified on Mercury: (1) they must be associated with a high-reflectance deposit having diffuse boundaries and (2) they must have a red spectral signature compared with surrounding terrain [*Head et al*., 2008, 2009; *Murchie et al*., 2008; *Robinson et al*., 2008; *Blewett et al*., 2009; *Kerber et al*., 2009, 2011] (e.g., Figure 1). These criteria also help to distinguish the identified candidate vents from collapse pit features, which have a similar morphology to the pyroclastic source vents but may be linked to endogenic activity unrelated to pyroclastic volcanism [e.g., *Gillis-Davis et al*., 2009]. Furthermore, it is important to note that any pyroclastic deposit that has had its associated source vent buried by younger material (e.g., volcanic flows or crater ejecta) would not be identified in this work. Such deposits could potentially be

©2014. American Geophysical Union. All Rights Reserved.

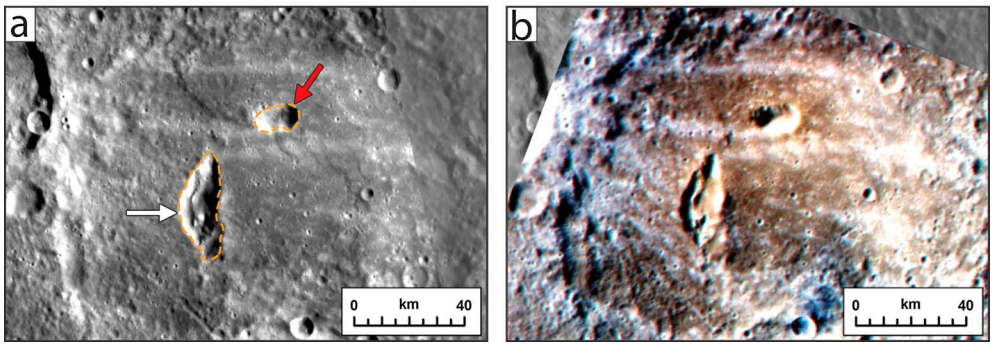


Figure 1. (a) Two newly identified pyroclastic deposits on the floor of Kipling crater (~160 km in diameter, centered at −18.5°N, 71.5°E) (Table 1). The vent at left center (white arrow) in the image is associated with the Kipling W deposit, and the upper vent (red arrow) is associated with the Kipling N deposit. Approximate vent outlines are indicated by dashed orange lines. MDIS NAC image EN9221974660M overlaid on a global mosaic obtained from MDIS NAC and WAC images with an average resolution of 250 m per pixel. (b) False-color MDIS WAC eight-band color image, for which red (R), green (G), and blue (B) are wavelengths 996.8 nm, 749 nm, and 430 nm, respectively; the "red" spectral signature of the Kipling N and W deposits is evident. The false-color image is from MDIS WAC images EW0221845266I–EW0221845286G, overlaid on the MDIS-derived global mosaic. North is up in both images.

identified from global MDIS color mosaics, in a manner similar to the technique employed by *Kerber et al*. [2011].

With these criteria, 10 newly identified pyroclastic deposits and corresponding source vents were added to the global catalog (Figure 2), along with the pyroclastic deposit located in the Tyagaraja crater identified by *Blewett et al*. [2011], bringing the total in the catalog to 51 deposits. The earlier convention for naming pyroclastic deposits [*Kerber et al*., 2011] was followed with the newly identified deposits (Table 1). As with the previous catalog [*Kerber et al*., 2011], the current catalog shows that pyroclastic deposits are relatively evenly distributed across the surface of Mercury and display minimal regional clustering (Figure 2). However, there does appear to be some degree of local clustering of pyroclastic deposits along the southern rim of the Caloris impact basin (Figure 2, cyan circle) as well as in and around large impact craters, such as Praxiteles (Figure 2, orange arrow) and Lermontov (Figure 2, green arrow) [*Head et al*., 2008, 2009; *Murchie et al*., 2008; *Kerber et al*., 2011]. Furthermore, all of the newly identified pyroclastic deposits are located in the interiors of impact craters and basins, with the exception of the N Rachmaninoff deposit, which is located in cratered terrain north of the Rachmaninoff basin. This

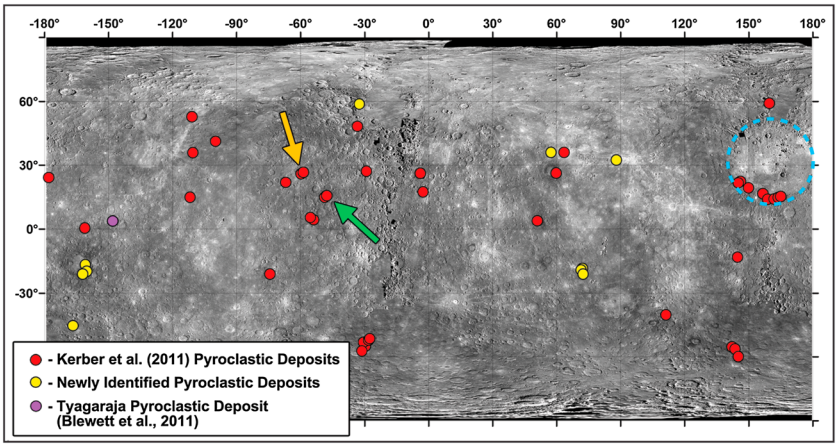


Figure 2. Locations of the 40 previously identified pyroclastic deposits (red circles) [*Kerber et al*., 2011], the 10 pyroclastic deposits newly identified here (yellow circles), and the Tyagaraja pyroclastic deposit (purple circle) [*Blewett et al*., 2011]. An approximate outline of Caloris basin is shown with a cyan dashed line, the location of Lermontov crater is indicated by a green arrow, and the location of Praxiteles crater is indicated by an orange arrow. The background is the MDIS-derived global mosaic introduced in Figure 1.

©2014. American Geophysical Union. All Rights Reserved.

Table 1. Names, Locations, and Deposit Areas of Newly Identified Pyroclastic Deposits

Deposit Name	Latitude (°N)	Longitude (°E)	Deposit Area (km^2)	Reference
Kipling N	−18.45	72.03	936	This work.
Kipling W	−19.21	71.43	1109	This work.
Kipling S	−21.16	72.40	1956	This work.
N Rachmaninoff	36.10	57.30	4273	This work.
Tolstoj E	−16.70	−161.70	4525	This work.
Tolstoj S	−21.13	−163.02	524	This work.
Tolstoj SE	−19.88	−161.14	512	This work.
Tyagaraja	3.75	−148.88	498	*Blewett et al.* [2011]
Unnamed crater 6	58.80	−32.90	1352	This work.
Unnamed crater 7	32.40	88.20	1383	This work.
Unnamed crater 8	−45.04	−167.60	484	This work.

distribution of deposits is consistent with the conclusion of *Kerber et al.* [2011] that pyroclastic deposits "are located principally on the floors of craters, along rims of craters, and along the edge of the Caloris basin."

4. Orbital Observations of Pyroclastic Deposits

Building on the earlier work of *Kerber et al.* [2011], we have analyzed the morphometry, global distribution, geologic associations, relative ages, and spectral characteristics of the pyroclastic deposits and associated source vents with the data sets described above.

4.1. Morphometry of the Source Vents and Pyroclastic Deposits

Three main aspects of morphometry were assessed in this study: source vent area, area of the associated pyroclastic deposits, and source vent depth. Areas of pyroclastic deposits were calculated for the 11 newly identified deposits, and source vent areas and depths were calculated for a subset of the entire catalog (i.e., both new and old source vents) from available MDIS and MLA data.

4.1.1. Areas of Source Vents and Deposits

Boundaries of source vents and pyroclastic deposits were mapped using MDIS NAC and WAC images. Areas were calculated from maps in a sinusoidal equal-area projection, which preserves area. High-resolution NAC and WAC images are not available for every vent at the illumination geometries most favorable for mapping topographic lows (such as the source vents), so we elected to map only 23 of the 51 source vents. The 23 mapped source vents have areas that range from ~60 to 800 km^2 (Table 2).

Table 2. Measured Vent Areas for Selected Pyroclastic Source Vents

Deposit Name	Vent Area (km^2)	Reference
Beckett	253	*Kerber et al.* [2011]
Geddes	488	*Pashai et al.* [2010]; *Kerber et al.* [2011]
Gibran	666	*Kerber et al.* [2011]
Glinka	199	*Kerber et al.* [2011]
Hemingway	148	*Kerber et al.* [2011]
Kipling W	405	This work.
Kipling S	245	This work.
Lermontov NE	79	*Kerber et al.* [2011]
Mistral NW	87	*Kerber et al.* [2011]
N Rachmaninoff	711	This work.
NE Derzhavin	339	*Kerber et al.* [2011]
NE Rachmaninoff	794	*Kerber et al.* [2011]
Picasso	653	*Kerber et al.* [2011]
Praxiteles NE	127	*Kerber et al.* [2011]
Praxiteles SW	237	*Kerber et al.* [2011]
RS-03	297	*Kerber et al.* [2011]
RS-05	356	*Kerber et al.* [2011]
Scarlatti	483	*Kerber et al.* [2011]
To Ngoc Van	327	*Kerber et al.* [2011]
Tolstoj E	149	This work.
Tolstoj S	61	This work.
Unnamed crater 1	176	*Kerber et al.* [2011]
Unnamed crater 5a	329	*Kerber et al.* [2011]

Areas for the 11 new pyroclastic deposits were mapped from MDIS WAC eight-filter color images on the basis of the high-reflectance and spectrally red signatures of the deposits. The newly identified deposits have a range of areas of ~480–4500 km^2 (Table 1), values that fall within the range of deposit areas mapped by *Kerber et al.* [2011]. As described by *Kerber et al.* [2011], these deposit sizes are large compared with those on the Moon and are even larger than their lunar counterparts when scaled for differences in surface gravitational acceleration. The larger pyroclastic deposits

©2014. American Geophysical Union. All Rights Reserved.

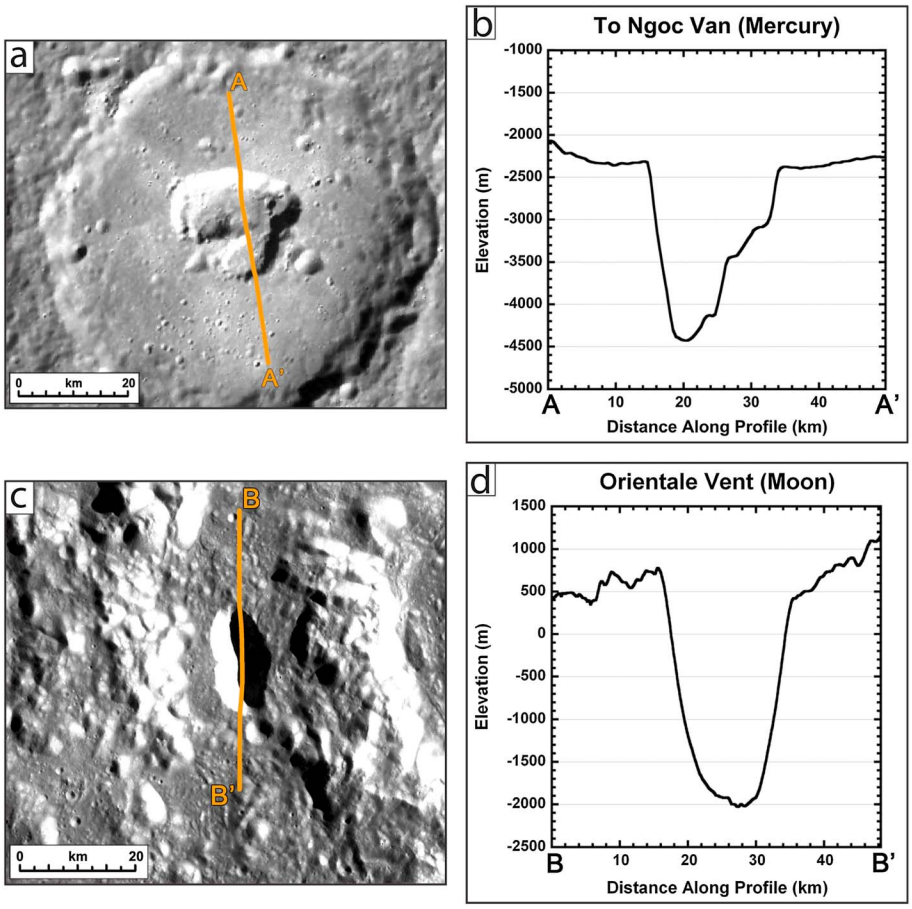


Figure 3. Topographic profiles of representative pyroclastic source vents on Mercury and the Moon. North is up in all images. (a) The To Ngoc Van pyroclastic source vent on Mercury at 52.8°N, −111.6°E [*Kerber et al.*, 2011]. The locus of an MLA topographic profile is indicated by the orange line, overlaid on the MDIS-derived global mosaic introduced in Figure 1. (b) MLA topographic profile of the To Ngoc Van vent along the line indicated in Figure 3a. The vent depth is ~2.1 km. The profile is from MLASCIRDR1105170905, and the topographic datum is a sphere of radius 2440 km. Vertical exaggeration is ~12.5:1. (c) The Orientale dark mantling deposit source vent [*Head et al.*, 2002]. The location of a Lunar Orbiter Laser Altimeter (LOLA) topographic profile is indicated by the orange line. The image is from a Lunar Reconnaissance Orbiter Camera global mosaic at a resolution of 100 m/pixel [*Robinson et al.*, 2010]. (d) LOLA [*Smith et al.*, 2010] topographic profile along the line indicated in Figure 3c. The vent depth is ~2.6 km. The profile is from LOLARDR_092020648, and the topographic datum is the gravitational equipotential surface evaluated at a radius of 1737.4 km from the spherical harmonic representation of the gravity field, evaluated to degree and order 60, given by *Mazarico et al.* [2012]. Vertical exaggeration is ~12.5:1.

on Mercury suggest that the erupting magma at the time of emplacement of these deposits had volatile contents that generally exceeded those of lunar magmas [*Kerber et al.*, 2011].

4.1.2. Vent Depths

Of the 51 identified pyroclastic deposits (Figure 2), as of this writing only six have been profiled by MLA (e.g., Figures 3a and 3b). Topographic profiles across these six vents show that the vent depths range from ~1.2 to 2.4 km (Table 3), with a mean depth of 1.8 km and a standard deviation of 0.4 km. The depths for the pyroclastic source vents indicated by MLA topographic data are in agreement with the depths of rimless depressions, both with and without identified pyroclastic deposits, determined from stereo-derived topography [*Gwinner et al.*, 2012]. The relatively narrow range of depths of ~1.2–2.4 km suggests either that the

Table 3. Measured Source Vent Depths for Pyroclastic Deposits With MLA Coverage

Deposit Name	Vent Depth (km)	Reference
Gibran	1.5	*Kerber et al.* [2011]
NE Derzhavin	1.7	*Kerber et al.* [2011]
NE Rachmaninoff	2.4	*Kerber et al.* [2011]
RS-02	1.2	*Kerber et al.* [2011]
Scarlatti	1.8	*Kerber et al.* [2011]
To Ngoc Van	2.1	*Kerber et al.* [2011]

©2014. American Geophysical Union. All Rights Reserved.

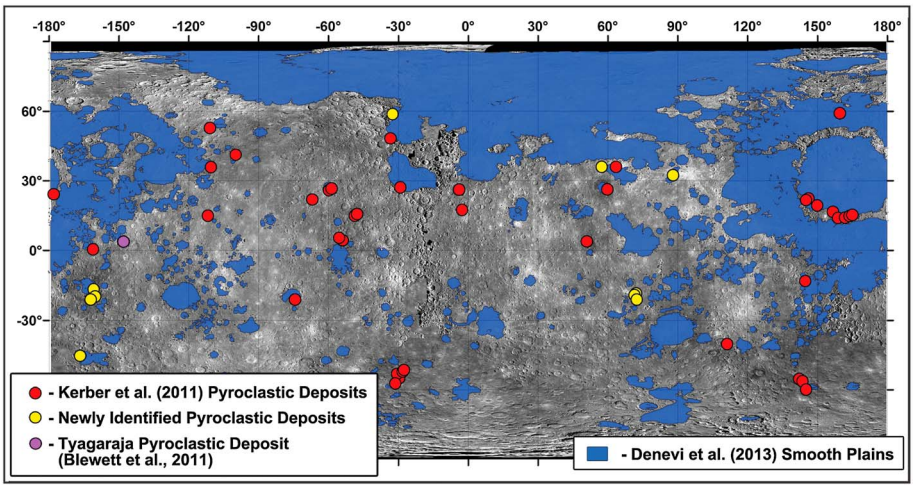


Figure 4. Distribution of pyroclastic deposits (as in Figure 1) compared with the distribution of smooth plains deposits mapped by *Denevi et al.* [2013] (blue regions). Note that the pyroclastic deposits are either distant from or located on the margins of the smooth plains units. The background is the MDIS-derived global mosaic introduced in Figure 1.

formation mechanism may control the final depth of the vent, or that these six data points do not span the full range of depth values.

4.2. Geologic Associations of Pyroclastic Deposits

An important aspect of the global distribution of these pyroclastic deposits is their association with different terrains and geologic features. The pyroclastic deposits typically occur within impact craters [*Kerber et al.*, 2011]; 46 of 51 (~90%) deposits occur in such settings. This strong correlation suggests a possible genetic link between impact cratering and the pyroclastic deposits.

We have also investigated the relation between pyroclastic deposits and the smooth plains deposits mapped by *Denevi et al.* [2013] (Figure 4). *Denevi et al.* [2013] interpreted the majority of smooth plains units to be volcanic in origin, and so an assessment of the relation between pyroclastic and plains deposits may elucidate aspects of the volcanological evolution of Mercury. On global to regional scales, most pyroclastic deposits are distant from smooth plains, but some pyroclastic deposits are found around the margins of smooth plains units, as earlier noted by *Denevi et al.* [2013]. The only large smooth plains unit to contain a pyroclastic deposit in its interior is the expanse of circum-Caloris plains to the north of the Caloris basin (Figure 4).

4.3. Relative Timing of Pyroclastic Activity

To assess the relative timing of the pyroclastic activity associated with these 51 pyroclastic deposits, each of the source vents was examined for crosscutting relationships. We found distinct crosscutting relationships at 14 pyroclastic source vents, and possible but less clear crosscutting relationships at 12 additional pyroclastic source vents. These relationships fall into three main categories. The first category is crosscutting by a secondary crater chain, a situation observed at only one site, the Praxiteles SW vent (Figure 5). The secondary crater chain crosscutting the Praxiteles SW vent can be traced back to the fresh, rayed impact crater Hokusai (~114 km in diameter, centered at 57.8°N, 16.9°E), which is located in the northern smooth plains [*Head et al.*, 2011] at a distance of ~2600 km.

The second type of relationship observed is crosscutting by contractional tectonic features (i.e., wrinkle ridges or lobate scarps). Clear relationships are observed at the NE Derzhavin (Figure 6a) and Glinka (Figure 6b) source vents, and more ambiguous relationships are observed at two other pyroclastic source vents, those associated with unnamed crater 1 (Figure 6c) and Geddes crater (Figure 6d) [*Pashai et al.*, 2010; *Kerber et al.*, 2011].

Lobate scarps are thought to be an expression of surface-breaking thrust faults [e.g., *Strom et al.*, 1975; *Watters et al.*, 1998]. At the NE Derzhavin site, the formation of Victoria Rupes appears to have caused the wall slump feature observed in the western portion of the NE Derzhavin vent (Figure 6a, yellow arrow). As crustal material was thrust over the vent during formation of Victoria Rupes, the vent may have provided

©2014. American Geophysical Union. All Rights Reserved.

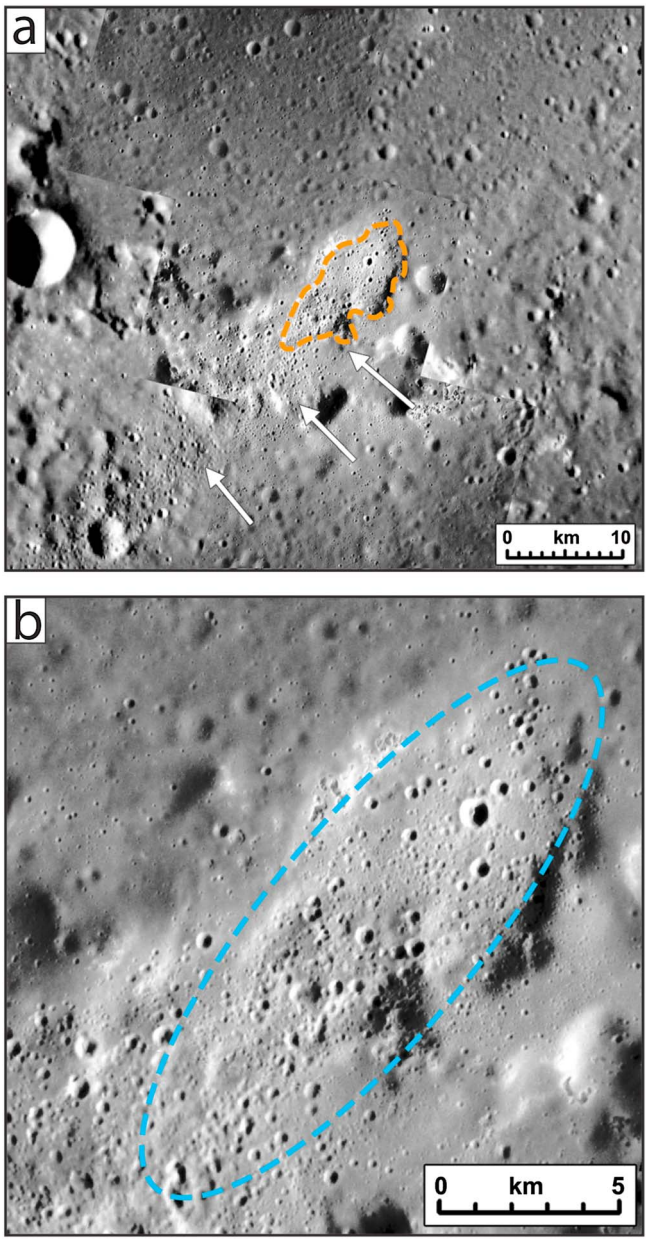


Figure 5. A secondary crater chain from the Hokusai impact crater cross-cuts the Praxiteles SW pyroclastic deposit and source vent at 26.0°N, −60.3°E [*Kerber et al.*, 2011]. North is up in both images. (a) Context image showing the Praxiteles SW pyroclastic deposit and source vent (approximate vent outline is indicated by dashed orange line) and the crosscutting secondary crater chain (indicated by white arrows). Mosaic of MDIS NAC images EN0223745081M, EN0223745074M, and EN0223745067M overlaid on the MDIS-derived global mosaic introduced in Figure 1. (b) Close-up view of the Praxiteles SW pyroclastic deposit source vent. Trend of crosscutting secondary crater chain is indicated by a cyan ellipse. Mosaic of MDIS NAC images EN0223745081M, EN0223745074M, and EN0223745067M.

accommodation space, permitting the collapse of a portion of the leading edge of the scarp into the vent. At the Glinka site, the lobate scarp is clearly observed to cut across the source vent rim as well as the vent floor (Figure 6b, yellow arrow). At unnamed crater 1 [*Kerber et al.*, 2011], no definitive crosscutting relationship is observed, although there may be an indication that the vent interior is crosscut by the associated scarp (Figure 6c, yellow arrow), an observation that is hindered by shadowing in the available NAC image. Similarly, at the Geddes site, the crisp morphology of the scarp (Figure 6d, red arrows) may suggest that it was not blanketed by pyroclastic material; however, no definitive crosscutting relationship is observable.

The third type of crosscutting relationship is between pyroclastic deposits and hollows, which are small depressions (on the order of tens to a few thousands of meters in diameter) with high-reflectance interiors and surrounding "halos" characterized by relatively "blue" spectra (i.e., reflectance increases less steeply with wavelength) [*Blewett et al.*, 2011, 2013; *Thomas et al.*, 2014]. At 11 of the 51 pyroclastic deposits, hollows clearly crosscut the pyroclastic vents and deposits (e.g., Figure 7, orange arrows), whereas another 11 of the pyroclastic deposits are possibly crosscut by hollows, with confirmation hindered by image resolution. In all cases for which adequate data exist, hollows appear to postdate the pyroclastic activity. It is also important to note that 29 of the 51 pyroclastic deposits show no association with hollows, and hollows are also found in many locations where there are no pyroclastic deposits [*Blewett et al.*, 2011, 2013; *Thomas et al.*, 2014].

To supplement crosscutting and stratigraphic relationships, planetary surfaces are commonly dated in both relative and absolute terms from the size-frequency distribution of superposed impact craters and a known or estimated impact crater production function [e.g., *Hartmann*, 1966, 1977; *Neukum et al.*, 1975]. However, dating pyroclastic deposits with such a method is not straightforward because the deposits are surficial and mantle the

©2014. American Geophysical Union. All Rights Reserved.

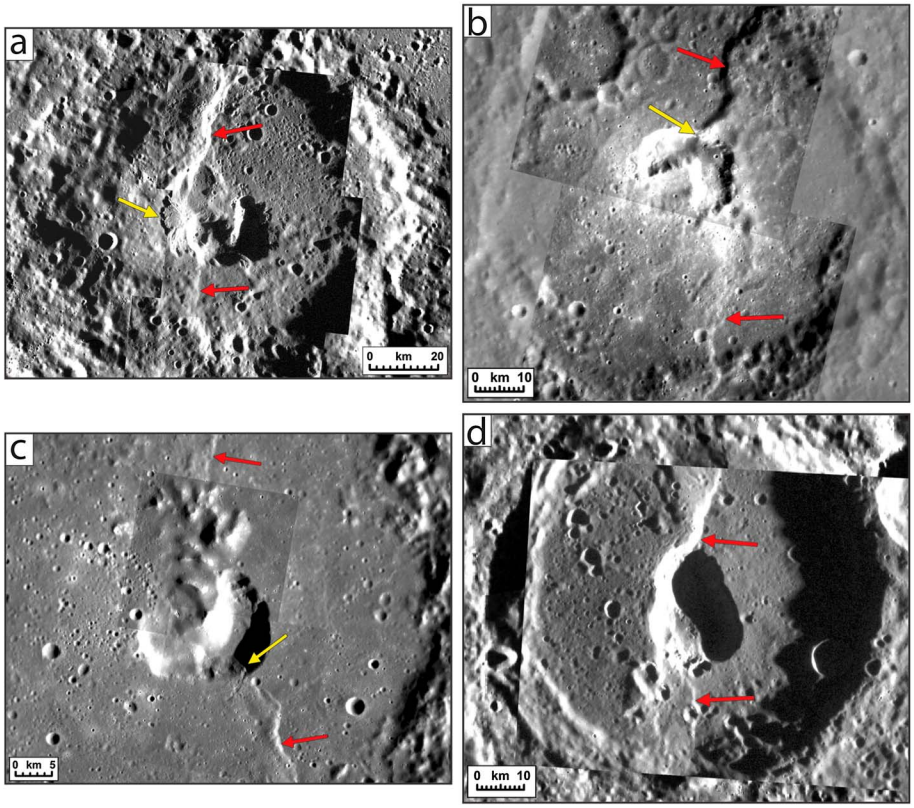


Figure 6. Crosscutting relationships between pyroclastic source vents and contractional tectonic structures, indicated by red arrows. North is up in all images. (a) Victoria Rupes (red arrows) crosscuts the NE Derzhavin pyroclastic source vent at 48.3°N, −33.8°E [*Kerber et al.*, 2011]. The yellow arrow indicates the slump feature caused by thrusting of material over the NE Derzhavin vent depression. Mosaic of MDIS NAC images EN0221237588M, EN0221237609M, and EN0221237630M overlaid on the MDIS-derived global mosaic introduced in Figure 1. (b) A lobate scarp (red arrows) crosscuts the Glinka pyroclastic source vent at 15.0°N, −112.4°E [*Kerber et al.*, 2011]. The scarp clearly cuts the Glinka vent rim at the point indicated by the yellow arrow. Mosaic of MDIS NAC images EN0242295873M and EN0242295825M overlaid on the global mosaic. (c) A lobate scarp (red arrows) crosscuts the pyroclastic source vent in unnamed crater 1 at 22.0°N, −67.5°E [*Kerber et al.*, 2011]. The scarp may crosscut the interior of the source vent at the location indicated by the yellow arrow. Mosaic of MDIS NAC images EN0239163782M, EN0223745181M, and EN0223745173M and MDIS WAC image EW0238909186G. (d) A lobate scarp (red arrows) crosscuts the Geddes pyroclastic deposit source vent at 27.2°N, −29.5°E [*Pashai et al.*, 2010; *Kerber et al.*, 2011]. MDIS NAC image EN0221107380M overlaid on the global mosaic.

underlying terrain, so it can be difficult to determine whether a crater is superposed on the pyroclastic deposit or the underlying surface. Further, the unconsolidated nature of the pyroclastic deposits can affect the size and preservation of impact craters [e.g., *Lucchitta and Schmitt*, 1974]. Moreover, the areas of the pyroclastic deposits are typically small, limiting the statistical precision of crater size-frequency distributions. These complications effectively prevent the derivation of relative or absolute crater retention ages for individual pyroclastic deposits.

Nonetheless, the fact that ~90% of these deposits occur within large impact craters can be used to assess their relative age. Large craters on the surface of Mercury are commonly degraded as a result of modification by several processes, including volcanism, tectonic deformation, emplacement of impact ejecta, and the formation of superposed craters [e.g., *Spudis and Guest*, 1988; *Watters et al.*, 2009; *Prockter et al.*, 2010, 2012; *Baker et al.*, 2011]. Therefore, assessing the degradation state of the host craters for the 46 pyroclastic deposits contained within them can offer some insight into their relative timing. Such an assessment was performed in this analysis with the qualitative classification of crater degradation, regarded as a proxy for relative crater age, of *Spudis and Guest* [1988]. Each crater that hosts a pyroclastic deposit was examined in MDIS images and assigned a crater degradation state. Those crater degradation classes are divided by geologic era [*Spudis and Guest*, 1988], and

©2014. American Geophysical Union. All Rights Reserved.

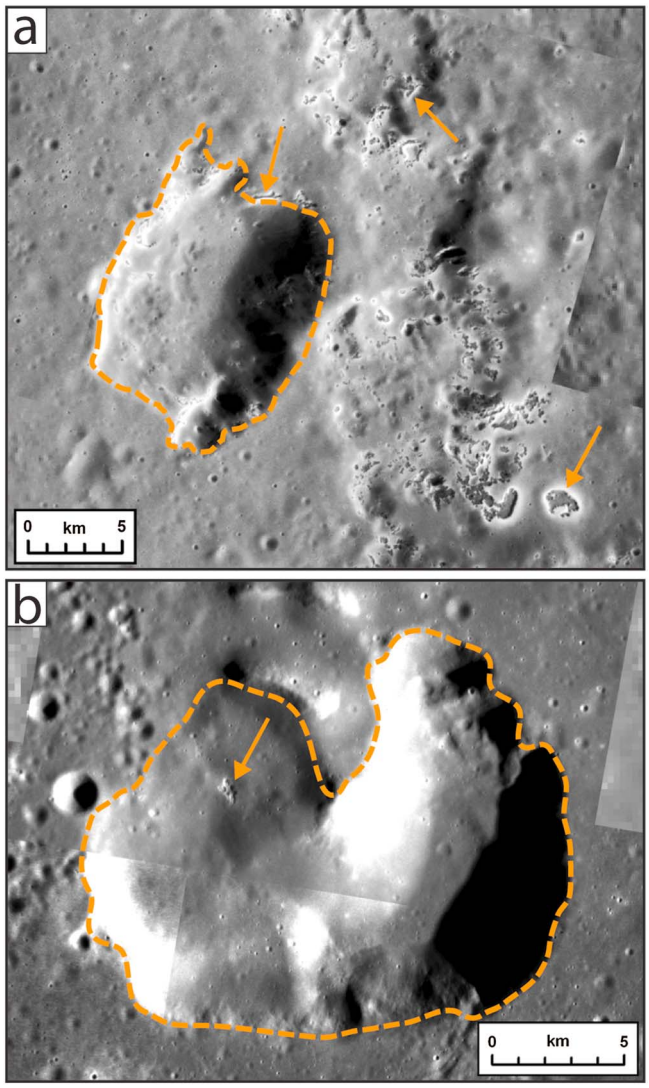


Figure 7. Examples of hollows crosscutting pyroclastic source vents and deposits. Approximate vent outlines are indicated by dashed orange lines. North is up in all images. (a) Hollows forming in the Praxiteles NE pyroclastic deposit and source vent at 26.7°N, −59.2°E [*Blewett et al*., 2011; *Kerber et al*., 2011]. Orange arrows indicate crosscutting hollows. Mosaic of MDIS NAC images EN0223831439M and EN0223831447M overlaid on the MDIS-derived global mosaic introduced in Figure 1. (b) Hollows forming in the unnamed crater 1 pyroclastic deposit source vent at 22.0°N, −67.5°E [*Kerber et al*., 2011]. Orange arrow indicates hollow superposed on the source vent floor. Mosaic of MDIS NAC images EN0223745181M, EN0223745173M, and EN0239163782M overlaid on the global mosaic.

examples of each of the classes (Mansurian, Calorian, Tolstojan, and Pre-Tolstojan) for impact craters hosting pyroclastic deposits are shown in Figure 8.

Results from the crater degradation assessment show that 10 pyroclastic deposits are hosted in Mansurian-age craters (~3.25–1 Ga), 13 deposits are hosted in Calorian-age craters (~3.9–3.25 Ga), 11 deposits are hosted in Tolstojan-age craters (~4–3.9 Ga), and two deposits are hosted in Pre-Tolstojan-age craters (>4 Ga) (Figure 9), where the ages indicated are estimates of the approximate age boundaries of each geological era inferred by extrapolation from the history of impact cratering on the Moon [*Spudis and Guest*, 1988]. The nine pyroclastic deposits located in Caloris were classified as being hosted in an impact feature at the Tolstojan-Calorian age boundary (as the Caloris impact basin defines this stratigraphic boundary) [*Spudis and Guest*, 1988], and the pyroclastic deposit in the Tolstoj basin was similarly classified as hosted by an impact feature at the boundary between Pre-Tolstojan and Tolstojan. Each pyroclastic deposit must be younger than its host crater, so the relative age of the host crater provides an upper limit on the age of each deposit.

4.4. Spectral Characteristics of Pyroclastic Deposits

Spectral characterization of the deposits was undertaken using data from the VIRS channel on the MASCS instrument. Of the 51 identified deposits, there are MASCS spectra for 39 as of this writing. The spectral signature of these deposits from MASCS is qualitatively consistent with that indicated by MDIS images [*Blewett et al*., 2009; *Kerber et al*., 2011], including a strongly red spectral slope (Figure 10a). However, apart from this spectral slope, there is little evident spectral character associated with these deposits. In particular, there is no resolvable crystal field absorption identifying the presence of octahedrally coordinated Fe^{2+} in silicate minerals, which manifests as a broad absorption band centered near 1000 nm [*Burns*, 1993a]. Although MASCS spectra are plotted here only to 800 nm (Figure 10), indications of a broad, 1000 nm crystal field absorption from minerals such as olivine and low-calcium pyroxene would have been visible even at these short wavelengths in laboratory spectra [e.g., *Adams*, 1974; *King and Ridley*, 1987; *Klima et al*., 2007, 2011]. Laboratory spectra are clearly optimal with respect

©2014. American Geophysical Union. All Rights Reserved.

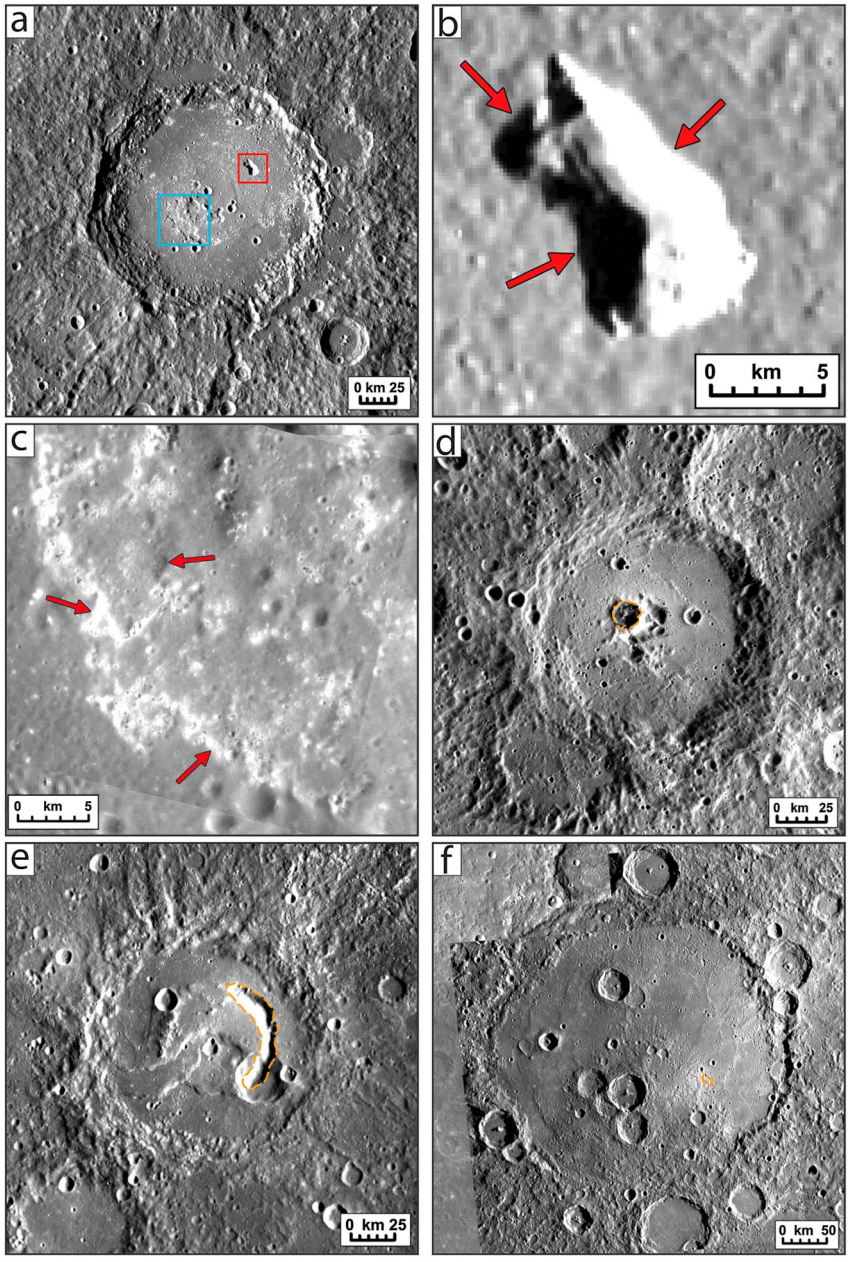


Figure 8. Different states of degradation of the host craters of selected pyroclastic deposits as identified with the crater degradation scheme of *Spudis and Guest* [1988]. North is up in all images. (a) The Lermontov NE and Lermontov SW pyroclastic deposits within the Mansurian-age Lermontov crater at 15.5°N, −48.6°E [*Kerber et al.*, 2011]. Note the different degradation states of the two pyroclastic deposit source vents, shown in more detail in Figures 8b and 8c, within the same crater, as indicated by the differing crispness of the vent edges, indicated by red arrows in Figures 8b and 8c. Mosaic of MDIS WAC images EW0228587466G and EW0243797322G overlaid on the MDIS-derived global mosaic introduced in Figure 1. (b) The Lermontov NE pyroclastic deposit source vent. The vent edges (red arrows) are comparatively crisp. The location of Figure 8b is indicated by a red box in Figure 8a. MDIS WAC image EW0228587466G. (c) The Lermontov SW pyroclastic deposit source vent. The vent edges (red arrows) are more degraded. The location of Figure 8c is indicated by a cyan box in Figure 8a. Mosaic of MDIS NAC images EN0223788445M and EN0223615672M overlaid on the global mosaic. (d) The Hemingway pyroclastic deposit within the Calorian-age Hemingway crater at 17.6°N, −2.9°E [*Kerber et al.*, 2011]. An approximate vent outline is indicated by the dashed orange line. Mosaic of MDIS NAC images EN0220847851M, EN0220804746M, EN0220804665M, and EN0220804578M overlaid on the global mosaic. (e) The Picasso pyroclastic deposit within the Tolstojan-age Picasso impact crater at 3.9°N, 50.9°E [*Kerber et al.*, 2011]. An approximate vent outline is indicated by the dashed orange line. Mosaic of MDIS NAC images EN0219476823M, EN0219476821M, EN0219476669M, and EN0219476667M overlaid on the global mosaic. (f) The Raphael pyroclastic deposit within the Pre-Tolstojan-age Raphael impact crater at −21.1°N, −74.9°E [*Kerber et al.*, 2011]. An approximate vent outline is indicated by the dashed orange line. Mosaic of MDIS WAC images EW0228587466G and EW0243797322G overlaid on the global mosaic.

©2014. American Geophysical Union. All Rights Reserved.

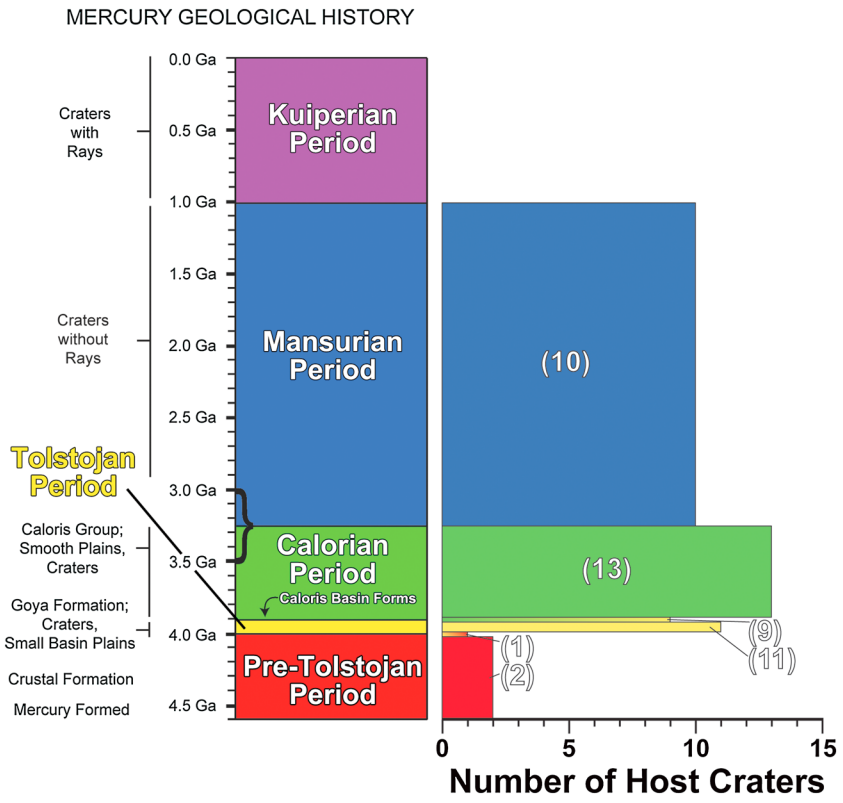


Figure 9. Results of the survey of host crater morphology for the 46 pyroclastic deposits located within impact craters. Shown are the major periods in Mercury's global stratigraphy [*Spudis and Guest*, 1988] and an approximate geological timescale for Mercury, modified from *Head et al.* [2007], on the left, and the number of pyroclastic deposits that are contained within host craters that have a degradation state comparable with craters from each geologic period as defined by *Spudis and Guest* [1988]. The nine deposits that fall at the Tolstojan-Calorian boundary are the nine deposits contained within the Caloris basin (which defines this stratigraphic boundary), and the deposit at the boundary between the Pre-Tolstojan and the Tolstojan is contained within the Tolstoj basin (which defines this stratigraphic boundary). Note the approximately even distribution of pyroclastic deposits hosted within older impact craters (e.g., Tolstojan) and younger impact craters (e.g., Mansurian).

to high signal-to-noise ratios, typically no mixing of different phases, and no space weathering, all of which are in contrast to the spacecraft data analyzed here; however, no broad absorption feature centered near 1000 nm is evident in the analyzed spectra. This observation is also consistent with previous findings [*Blewett et al.*, 2009; *Kerber et al.*, 2011].

A common technique when looking at spectra of planetary surfaces is to ratio the data to spectrally neutral background terrain [e.g., *McCord et al.*, 1972, 1981]. This technique brings out the spectral diversity in an area of interest and accentuates any potential spectral features or absorptions and has been used previously for MASCS spectral analysis [*McClintock et al.*, 2008; *Izenberg et al.*, 2014]. Each of the spectra from the 39 pyroclastic deposits with MASCS coverage was ratioed to a spectrum from a nearby region exterior to the pyroclastic deposit but acquired during the same orbit (Figures 10b and 10c).

The exterior spectra used for ratioing were manually examined and selected on the basis of their similarity in absolute reflectance and spectral shape to the average MASCS/VIRS global spectral signature [*Izenberg et al.*, 2014], which is an average of all MASCS/VIRS spectra from the primary and first extended missions of the MESSENGER spacecraft that satisfy the following restrictions: incidence angle $< 70°$, emission angle $< 80°$, phase angle $< 95°$, detector temperature $< 35°C$, and number of spectra in the observation > 20. The spectral detector pixels were also binned by four for this mean spectrum from the VIS detector [*Izenberg et al.*, 2014]. The similarity to the MASCS/VIRS global average spectrum was assessed by examining the ratio of the exterior spectra to the global average and searching for spectra with values of approximately 1 across the wavelength range of interest (i.e., 300–800 nm).

©2014. American Geophysical Union. All Rights Reserved.

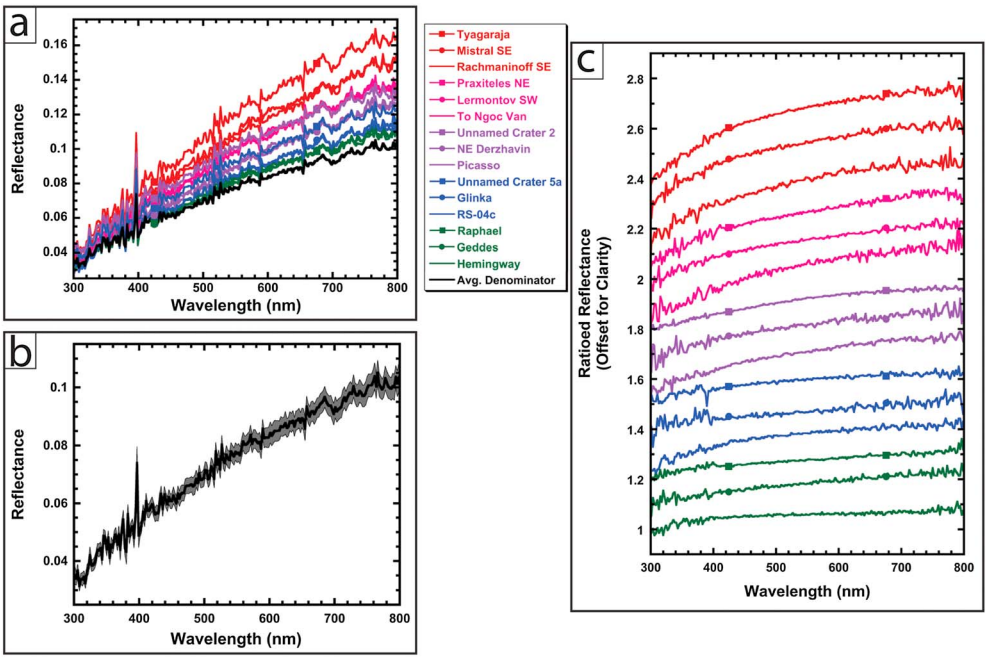


Figure 10. Example MASCS spectra of 15 pyroclastic deposits showing the general spectral characteristics of these deposits. (a) Geometrically corrected reflectance spectra for 15 different pyroclastic deposits, as well as the average of the 39 spectra of surrounding terrain used for ratioing (black line; see also Figure 10b). Note that all the spectra have higher reflectance and a steeper spectral slope than the average spectrum of surrounding terrain. MASCS orbit numbers for the plotted spectra are listed in Table 4. (b) Plot of the average of the 39 spectra of terrain surrounding the pyroclastic deposits (thick black line). Shaded area indicates the 1-standard-deviation bounds on this average. Note the relatively narrow range for spectra of surroundings. (c) Ratioed MASCS spectra for the 15 pyroclastic deposits shown in Figure 10a. The reference spectrum in each case is that of surrounding terrain that has a spectrum near the global average for Mercury [*Izenberg et al.*, 2014] obtained during the same orbit. Note the range in spectral characteristics, although all deposits have a red spectral slope and variable degrees of a turndown in the UV. Spectra are offset for clarity.

Although different spectra were used for determining the ratioed reflectance from each pyroclastic deposit, all of these ratios approximate a ratio to the global average MASCS/VIRS spectrum [*Izenberg et al.*, 2014]. A plot of the average of the 39 denominator spectra with 1-standard-deviation bounds (Figure 10b) shows that there is minimal variability among denominator spectra, and thus the adopted procedure allows for interdeposit comparison of ratioed reflectance spectra.

Table 4. MASCS Orbit Numbers for the Spectra Displayed in Figure 10

Deposit Name	Orbit Number	Reference
Geddes	ORB_11274_091908	*Kerber et al.* [2011]
Glinka	ORB_11312_221408	*Kerber et al.* [2011]
Hemmingway	ORB_12073_223244	*Kerber et al.* [2011]
Lermontov SW	ORB_11247_091659	*Kerber et al.* [2011]
Mistral SE	ORB_11103_161453	*Kerber et al.* [2011]
NE Derzhavin	ORB_11099_154240	*Kerber et al.* [2011]
Picasso	ORB_11257_165554	*Kerber et al.* [2011]
Praxiteles NE	ORB_11106_043345	*Kerber et al.* [2011]
Rachmaninoff SE	ORB_11226_085956	*Kerber et al.* [2011]
Raphael	ORB_11109_122433	*Kerber et al.* [2011]
RS-04c	ORB_11359_131457	*Kerber et al.* [2011]
To Ngoc Van	OB2_12123_230528	*Kerber et al.* [2011]
Tyagaraja	ORB_11346_063128	*Blewett et al.* [2011]
Unnamed crater 2	ORB_11346_012509	*Kerber et al.* [2011]
Unnamed crater 5a	ORB_11336_233947	*Kerber et al.* [2011]

From the spectral ratioing technique, the pyroclastic deposits are seen again to be spectrally redder than their surrounding terrain (Figure 10c). However, the steepness of the slope of the ratioed spectra is variable. Some deposits have a weakly red slope whereas some have a strongly red slope in the ratioed data; slope values over visible wavelengths in the ratioed spectra range over an order of magnitude (Figure 10c). Additionally, all of the pyroclastic deposits, with the exception of the unnamed crater 4 deposit [*Kerber et al.*, 2011], have mean ratioed reflectance values >1 across the wavelength region ~300–800 nm,

©2014. American Geophysical Union. All Rights Reserved.

again indicating that they are brighter than the surrounding terrain (Figure 10a). The mean relative reflectance value for the unnamed crater 4 deposit is slightly less than 1, but this deposit appears brighter than the surrounding terrain in MDIS eight-filter color images, so this low relative reflectance value may be due to the precise location of the MASCS footprint in relation to the pyroclastic deposit itself (i.e., the footprint may include both portions of the bright pyroclastic deposit and darker surrounding material). Alternatively, this observation may be the result of the specific choice of background terrain used in ratioing for this individual deposit.

In addition to the red spectral slope, for many of the ratioed spectra there appears to be a downturn in the ratioed reflectance values at ultraviolet wavelengths, shortward of ~400 nm (Figure 10c). The UV downturn is seen with varying degrees of strength in the ratioed reflectance data (Figure 10c). To quantify this spectral feature, we define the spectral parameter

$$\mathrm{UV_{depth}} = \mathrm{Depth_{300}} + \mathrm{Depth_{325}} + \mathrm{Depth_{350}}, \tag{1}$$

which uses the formulations

$$\mathrm{Depth_{300}} = \left\{[R(401)]\text{–}[401-303]\ \mathrm{VIS_{slope}}\right\}/[R(303)], \tag{2}$$

$$\mathrm{Depth_{325}} = \left\{[R(401)]\text{–}[401-324]\ \mathrm{VIS_{slope}}\right\}/[R(324)], \tag{3}$$

$$\mathrm{Depth_{350}} = \left\{[R(401)]\text{–}[401-350]\ \mathrm{VIS_{slope}}\right\}/[R(350)], \tag{4}$$

and

$$\mathrm{VIS_{slope}} = \{[R(550)] - [R(750)]\}/\{550-750\}, \tag{5}$$

where $R(\lambda)$ is the ratioed reflectance value at the wavelength λ given in nanometers. To avoid spurious results from channel-to-channel instrument noise, a running average of ratioed reflectance values from three adjacent spectral channels was used in calculating the parameters in the above expressions, with the averages centered on the wavelengths listed in equations (2)–(5). The spectral parameter given by equation (1) approximately maps the fractional strength of the UV downturn in the ratioed spectral data by calculating the ratio of the expected ratioed reflectance value at 300, 325, and 350 nm from the visible wavelength slope ($\mathrm{VIS_{slope}}$) to the actual ratioed reflectance value at these wavelengths. Spectra with stronger UV downturns (i.e., steeper UV slopes) will have a higher $\mathrm{UV_{depth}}$ parameter value.

With this $\mathrm{UV_{depth}}$ parameter, we have classified the MASCS spectra of the pyroclastic deposits into four spectral types, types I to IV (Figure 11). These types were distinguished on the basis of the mean (μ_{UV}) and standard deviation (σ_{UV}) of the calculated $\mathrm{UV_{depth}}$ values (~3.11 and 0.08, respectively):

$$\text{For type I, } \mathrm{UV_{depth}} < \mu_{\mathrm{UV}} - \sigma_{\mathrm{UV}}$$

$$\text{For type II, } \mu_{\mathrm{UV}} - \sigma_{\mathrm{UV}} \le \mathrm{UV_{depth}} < \mu_{\mathrm{UV}}$$

$$\text{For type III, } \mu_{\mathrm{UV}} \le \mathrm{UV_{depth}} < \mu_{\mathrm{UV}} + \sigma_{\mathrm{UV}}$$

$$\text{For type IV, } \mu_{\mathrm{UV}} + \sigma_{\mathrm{UV}} \le \mathrm{UV_{depth}}$$

Type I spectra typically have a red spectral slope and minimal UV downturn, type II spectra typically have a slightly redder spectral slope with a weak UV downturn, type III spectra typically have a still redder spectral slope and a clear UV downturn, and type IV spectra typically have the steepest red spectral slope and the strongest UV downturn (Figure 11). The absolute reflectance values for these four types also increases from type I to type IV (Figure 11), and plotting the $\mathrm{UV_{depth}}$ parameter versus absolute reflectance at 700 nm (i.e., unratioed reflectance) shows a clear positive correlation (Figure 12). This relationship is approximately linear (with a squared correlation coefficient $r^2 = 0.61$), suggesting that the process that contributes to a weaker UV downturn also results in a darkening of the deposit material.

©2014. American Geophysical Union. All Rights Reserved.

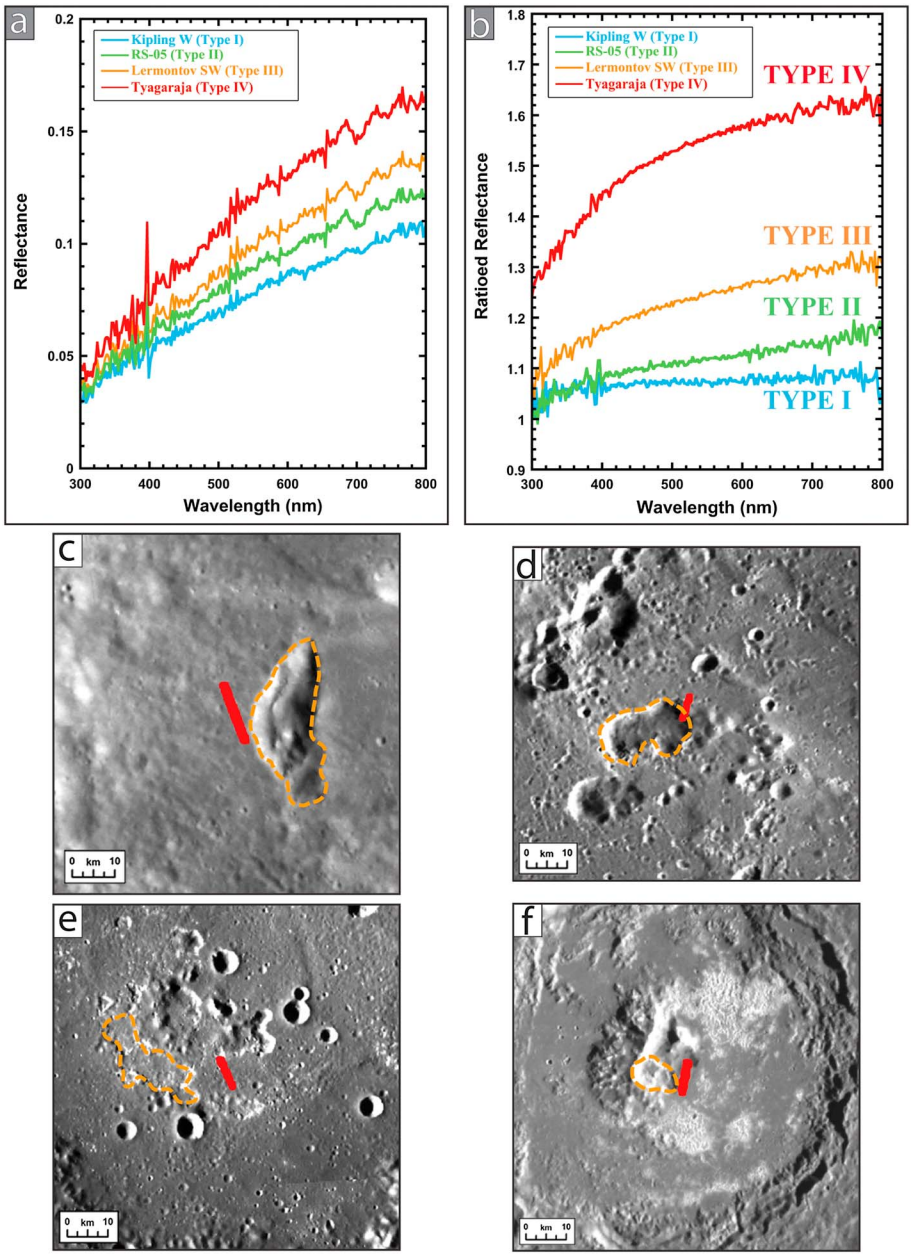


Figure 11. MASCS spectra showing examples of the four different spectral types (types I–IV). (a) Geometrically corrected reflectance for the Kipling W pyroclastic deposit (type I), RS-05 pyroclastic deposit (type II), Lermontov SW pyroclastic deposit (type III), and Tyagaraja pyroclastic deposit (type IV) [*Blewett et al.*, 2011; *Kerber et al.*, 2011]. Spectra are from MASCS orbital tracks ORB_11222_205837, ORB_11354_152144, ORB_11247_091659, and ORB_11346_063128 for the Kipling W, RS-05, Lermontov SW, and Tyagaraja pyroclastic deposits, respectively. (b) Ratioed MASCS spectra for the four spectra shown in Figure 11a. The reference spectrum in each case is that of surrounding terrain that has a spectrum near the global average for Mercury [*Izenberg et al.*, 2014] obtained during the same orbit. Note the change from a weakly red spectral slope and minimal to no UV downturn for type I to a strongly red spectral slope and strong UV downturn for type IV. (c–f) Locations of MASCS footprints on Mercury's surface (indicated by filled red boxes) for the spectra shown in Figure 11a and used as the numerators for the ratioed spectra in Figure 11b, for the (Figure 11c) Kipling W, (Figure 11d) RS-05, (Figure 11e) Lermontov SW, and (Figure 11f) Tyagaraja pyroclastic deposits. Approximate vent outlines are indicated by dashed orange lines. Background for all images is the MDIS-derived global mosaic introduced in Figure 1.

©2014. American Geophysical Union. All Rights Reserved.

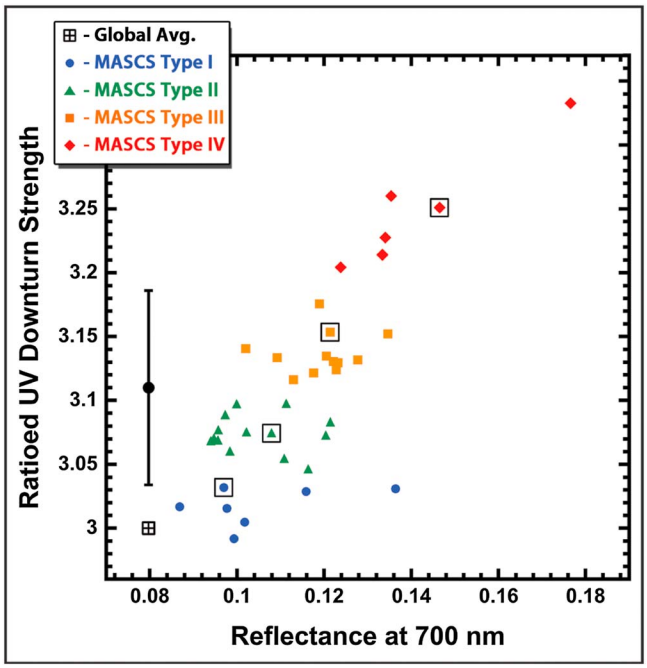


Figure 12. Ratioed UV downturn strength (i.e., UV_{depth} parameter value) versus absolute reflectance at 700 nm for the 39 deposits with MASCS spectral coverage. Note the positive correlation between the UV downturn strength and absolute reflectance at 700 nm ($r^2 = 0.61$). Plotted reflectance values are an average of three spectral channels centered on ~700 nm in an attempt to reduce spurious results from channel-to-channel instrument noise. Black dot indicates the average UV downturn strength (μ_{UV}); error bars denote ± 1 standard deviation (σ_{UV}). Boxes around individual points identify the example spectrum of each type shown in Figure 11.

Although we have used the UV_{depth} parameter to classify the spectra of pyroclastic deposits into four spectral types, it is important to note that the population of spectra is not separable into four distinct spectral groups (Figures 10a and 12). Rather, our classification scheme constitutes a spectral sorting of the spectra of pyroclastic deposits on the basis of the statistics of the UV_{depth} parameter. The assignment of four spectral types has been designed more to search for systematic patterns in the spectral signatures of the pyroclastic deposits than to identify distinctive spectral units.

The geographic distribution of the four different spectral types (Figure 13) does not indicate a high degree of clustering, as the four types are spread relatively evenly across the surface. This distribution suggests that the continuum in spectral shapes is not geographically controlled. The frequency distribution of the four spectral types (Figure 13, inset) appears normally distributed, a pattern that reflects how the types were defined (i.e., using μ_{UV} and $\mu_{UV} \pm \sigma_{UV}$ as the limits).

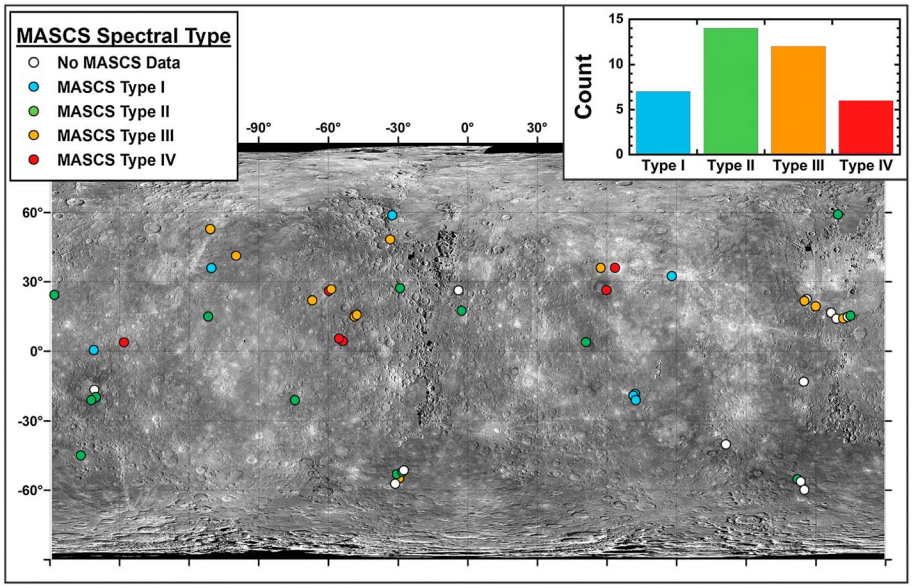


Figure 13. Distribution of the four different spectral types of pyroclastic deposits identified in this work (Figure 11). White circles denote locations with no MASCS data, blue circles indicate type I deposits, green circles indicate type II deposits, orange circles indicate type III deposits, and red circles indicate type IV deposits. Note the relatively even distribution of the four spectral types. Background is the MDIS-derived global mosaic introduced in Figure 1. Inset shows a histogram of number of occurrences of each type of pyroclastic deposit.

©2014. American Geophysical Union. All Rights Reserved.

5. Discussion

On the basis of the orbital observations of pyroclastic deposits presented above, we may draw several inferences about the nature and timing of pyroclastic volcanic activity on Mercury.

5.1. Vent Morphometry

The measured areas for the 23 confidently mapped source vents (Table 2) show that these vents are large, comparable in size to terrestrial calderas formed from large plinian eruptions [e.g., *Lipman*, 1997; *Geyer and Martí*, 2008]. This size range then raises the question of whether the depressions present at the center of the pyroclastic deposits are actually vents or are instead calderas formed by the posteruption collapse of the surface. Future work involving detailed stratigraphic mapping of individual events coupled with investigation of high-spatial-resolution stereo-derived topography for these vents will help to address this question [e.g., *Gwinner et al*., 2012].

Although vent areas are similar to those of terrestrial calderas from explosive volcanic activity, vent depths have a relatively narrow range of ~1.2–2.4 km (Figures 3a and 3b and Table 3), and the vents are ~2–5 times deeper than terrestrial calderas formed by large plinian eruptions [e.g., *Lipman*, 1997]. The dimensions of terrestrial and mercurian volcanic features cannot be compared easily, however, as many factors are involved, including not only the difference in gravitational acceleration but also possible differences in the volume of magma present beneath any one feature, the volatile content of that magma, and the availability of shallow crustal volatiles with which it might interact.

A closer analog to the pyroclastic source vents on Mercury may be vent depressions associated with some pyroclastic deposits on the Moon. The Orientale dark mantling deposit (Figure 3c) is a "ring" deposit of pyroclastic material in the Orientale basin on the Moon interpreted to have been deposited via vulcanian-style volcanism [*Head et al*., 2002]. This source vent has a measured area of ~148 km^2 [*Head et al*., 2002], which falls within the range of areas of pyroclastic source vents on Mercury (Table 2), and its depth is ~2.6 km (Figure 3d), also similar to the depths of pyroclastic source vents on Mercury (Table 3). As with terrestrial analogs for the mercurian source vents, it is difficult simply to compare the two features without more detailed considerations. These morphometric similarities would benefit from a more detailed volcanological analysis [e.g., *Jozwiak and Head*, 2012; *Wilson and Head*, 2012]. Another interesting aspect that will be illuminated by future detailed studies on individual vent morphologies is whether the measured vent areas and depths are representative of solely the eruption of pyroclastic material, or if there have been multiple episodes of activity, including vent collapse, at a given source vent.

5.2. Vent Associations With Impact Craters

There is a strong correlation between pyroclastic deposits and impact craters, with 46 of 51 (~90%) pyroclastic deposits found in this geological context. Impact bombardment pervasively fractured the upper crust and locally reduced the crustal thickness beneath large impact basins; both of these processes may have aided the upward propagation of magma-filled dikes to the surface [e.g., *Head and Wilson*, 1992]. These effects may account for the observation that pyroclastic activity is predominantly confined to the interiors of impact craters.

Previous work on the ascent and eruption of magma on Mercury has suggested that the thermal contraction of the planet is likely to have led to a global stress state marked by horizontal compression, making it difficult for magma to reach the surface [*Strom et al*., 1975; *Wilson and Head*, 2008, 2012]. Such a stress state may help to account for the localization of pyroclastic deposits within impact craters, on the grounds that crater formation may have served to relieve the preexisting stress in the target area and create easier pathways for ascending magma to reach the surface beneath impact craters [e.g., *Head and Wilson*, 1992].

5.3. Vent Associations With Smooth Plains

It is clear that most pyroclastic deposits are far from the smooth plains deposits mapped by *Denevi et al*. [2013], although a minority of the deposits are clustered around the margins of the smooth plains units (Figure 4). The only pyroclastic deposit contained within a large expanse of smooth plains is RS-02 [*Kerber et al*., 2011], which is located to the north of the Caloris basin, in the middle of a large area of circum-Caloris plains (Figure 4). *Denevi et al*. [2013] interpreted the majority of mapped smooth plains as volcanic in origin,

©2014. American Geophysical Union. All Rights Reserved.

but they noted that a volcanic origin is much less clear for the circum-Caloris plains to the north and west of the basin. It is therefore possible that pyroclastic deposit RS-02 is not located within a volcanic unit.

The concentration of several pyroclastic deposits around the margins of large smooth plains deposits (Figure 4) parallels the distribution of lunar pyroclastic deposits, which are often located around the margins of large mare deposits [e.g., *Head and Wilson*, 1979; *Gaddis et al*., 1985; *Weitz et al*., 1998]. One possible explanation for this observation is that there is a genetic relationship between the two types of volcanism, whereby the same period of volcanic activity was responsible for the emplacement of the smooth plains and the adjacent pyroclastic materials. Such a scenario, for instance, has been proposed for the Alphonsus crater pyroclastic deposits on the Moon. Under that scenario, the magma source that fed the emplacement of the nearby Mare Nubium deposit may have also contributed magma beneath the Alphonsus crater, which then reached the surface in one or more vulcanian eruptions to form the pyroclastic deposits [*Head and Wilson*, 1979].

However, many of the pyroclastic deposits on Mercury are not associated with smooth plains deposits (Figure 4). For these deposits, it is likely that another factor is controlling their location, such as the characteristics (e.g., volatile content) of the mantle source region or the presence of a recently formed impact crater, as discussed above. Such alternative controls are likely to be most important for the younger pyroclastic deposits (i.e., those observed within Calorian and Mansurian impact craters; Figures 8 and 9), as *Denevi et al*. [2013] concluded that the majority of the volcanic smooth plains were emplaced from ~3.9 to 3.7 Ga.

The lack of pyroclastic deposits identified on the large expanses of smooth plains mapped by *Denevi et al*. [2013] does not imply that pyroclastic volcanism never occurred in these regions. Rather, one may conclude only that there has been no pyroclastic activity in these regions subsequent to the emplacement of the smooth plains deposits. Given that pyroclastic activity appears to have occurred into the Mansurian (Figures 8 and 9), however, long after the emplacement of the majority of the smooth plains deposits at ~3.9–3.7 Ga [*Denevi et al*., 2013], there is likely to be a physical explanation for the absence of pyroclastic deposits in smooth plains regions. One possibility, for instance, is that the volatiles needed to drive explosive volcanic eruptions were removed from the mantle source regions of the plains deposits during the partial melting and magma transport that led to the eruptions of the plains-forming lavas.

5.4. Relative Timing of Pyroclastic Volcanism

Another important aspect of pyroclastic deposits is their relative ages of emplacement inferred on the basis of both observed crosscutting relationships (Figures 5–7) and the degradation state of the host impact craters (Figures 8 and 9).

The secondary crater chain from the Hokusai impact crater that is observed to crosscut the Praxiteles SW vent (Figure 5) places the cessation of pyroclastic activity at the Praxiteles SW vent earlier than the impact that formed the Hokusai crater, which is of Kuiperian age on the basis of its extensive system of well-preserved rays [*Spudis and Guest*, 1988].

Additionally, the observed crosscutting of two pyroclastic source vents by lobate scarps (Figures 6a and 6b, yellow arrows) indicate that the pyroclastic activity at the NE Derzhavin and Glinka sites ended prior to the final major episode of activity along these tectonic features.

Many of the contractional tectonic features on Mercury, such as these lobate scarps, are believed to have resulted from an extended period of global contraction [*Strom et al*., 1975; *Watters et al*., 1998] resulting from the cooling of the planet's interior [e.g., *Hauck et al*., 2004]. This period of global contraction is thought to have initiated relatively early in Mercury's history [*Strom et al*., 1975; *Watters et al*., 1998], but many of the larger contractional landforms may be associated with faults that continued to be active until much more recently in Mercury's geological history [e.g., *Banks et al*., 2012]. Since the crosscutting relationships observed here imply only that pyroclastic activity at these two sites ended prior to the final movement along the lobate scarps, and not necessarily prior to the time of their initiation, it is unclear where these deposits fall in Mercury's global stratigraphy. Thus, it is difficult to constrain the relative age of the pyroclastic activity at the NE Derzhavin and Glinka sites from the observed crosscutting relationships with lobate scarps alone.

The clear crosscutting of 11 pyroclastic source vents by hollows (e.g., Figure 7, orange arrows) is consistent with the hypothesis that hollows are geologically young features that may even be currently active on the surface of Mercury at some locations [*Blewett et al*., 2011]. The superposition relations suggest that the

©2014. American Geophysical Union. All Rights Reserved.

pyroclastic activity at these 11 sites ceased before the final development of the current population of hollows, but they do not preclude the possibility that these pyroclastic deposits may also be geologically young.

As hollows are thought to form through some sort of material removal process [*Blewett et al*., 2011, 2013; *Vaughan et al*., 2012; *Thomas et al*., 2014], it is possible that the hollows are forming either in the pyroclastic deposit material or in the material that underlies the pyroclastic deposits. The observations presented here do not favor either of these scenarios, so further work on the relation between pyroclastic deposits and hollows with high-spatial-resolution NAC images and stereo-derived topography [e.g., *Gwinner et al*., 2012] is warranted to address this question.

That a number of the identified pyroclastic deposits are crosscut by hollows may be related to the idea that both geologic features are associated with volatiles [e.g., *Kerber et al*., 2009, 2011; *Blewett et al*., 2011; *Thomas et al*., 2014]. However, given that both pyroclastic deposits and hollows are primarily found within impact craters [e.g., *Blewett et al*., 2011, 2013; *Kerber et al*., 2011; *Vaughan et al*., 2012; *Thomas et al*., 2014], the spatial relation may be more coincidental than causal. More detailed analyses of both types of features and the development of additional models of hollow formation [e.g., *Vaughan et al*., 2012] would be helpful to explore this connection further.

The degradation states of the craters that host pyroclastic deposits provide upper limits on the ages of the pyroclastic deposits relative to Mercury's global stratigraphy [*Spudis and Guest*, 1988] and are likely to provide the best constraints on the relative timing of pyroclastic activity on the surface of Mercury. If, for example, a pyroclastic deposit occurs within a Mansurian-age crater, it can be concluded that the pyroclastic activity at that site must be Mansurian or younger.

The results of this survey (Figure 9) show that the 46 pyroclastic deposits within impact craters have host craters with a range of stratigraphic ages, from Mansurian to Pre-Tolstojan, according to the degradation criteria of *Spudis and Guest* [1988], with approximately equal numbers of Mansurian, Calorian, and Tolstojan host craters. We can therefore rule out the possibility that all of the pyroclastic activity occurred early in Mercury's history.

It is more difficult to rule out the possibility that all of the pyroclastic activity occurred relatively recently in Mercury's history, because this scenario would result in more pyroclastic deposits in older host craters, if only because there are more older craters on Mercury, and such a relation is similar to what is observed (Figure 9). However, the pyroclastic source vents themselves have different degradation states, and those states of preservation can vary even across a single host crater (e.g., Figures 8b and 8c). These observations lead us to conclude that the pyroclastic activity on Mercury is likely to have occurred over a considerable fraction of the planet's history, with some deposits emplaced early and some deposits more recently.

5.5. Spectral Characteristics of Pyroclastic Deposits and Potential Causes for the UV Downturn

The spectral reflectance of the pyroclastic deposits (Figures 10 and 11) is characterized by relatively high reflectance values, a red spectral slope, and no resolvable broad absorption feature centered near 1000 nm, consistent with previous spectral characterizations of these deposits [*Blewett et al*., 2009; *Kerber et al*., 2011]. Although MASCS spectra are primarily analyzed from 300 to 800 nm (Figures 10 and 11), the crystal field absorption band centered near 1000 nm in spectra of mafic minerals such as olivine and low-calcium pyroxene is broad in nature, and some indication of such an absorption should appear even at these short wavelengths, as evidenced in laboratory spectra [e.g., *Adams*, 1974; *King and Ridley*, 1987; *Klima et al*., 2007, 2011]. Despite the fact that MASCS spectra differ from laboratory spectra, which are typically acquired under more favorable measurement conditions, the lack of a resolvable broad absorption centered near 1000 nm in the pyroclastic deposit spectra indicates that there is a low concentration (less than a few weight percent) of octahedrally coordinated Fe^{2+} present in the crystal structure of silicate minerals in the deposits [*Burns*, 1993a]. This conclusion is consistent with the elemental abundances measured by MESSENGER's X-Ray Spectrometer (XRS) and Gamma-Ray Spectrometer, which indicate Fe abundances everywhere less than ~4 wt % [*Nittler et al*., 2011] and averaging ~1.9 wt % in the northern hemisphere [*Evans et al*., 2012].

Ratios of the spectra of pyroclastic deposits to spectra of surrounding terrain having spectral characteristics similar to the average reflectance for Mercury [*Izenberg et al*., 2014] reveal a downturn at wavelengths shortward of ~400 nm. The strength of this UV downturn differs among pyroclastic deposits (Figure 11b) and also appears to be correlated with absolute reflectance values (Figure 12). Several factors could potentially cause such a spectral feature, and we mention three possibilities here: (1) the transition metal content of the deposits, (2) the grain size of the deposits, and (3) the degree of space weathering of the deposits.

©2014. American Geophysical Union. All Rights Reserved.

Spectral absorption features at UV wavelengths in geologic materials are primarily caused by oxygen-metal charge transfer (OMCT) bands from transition metals in the silicate mineral structure [*Burns*, 1993b]. These OMCT bands are typically centered at ~200–300 nm, depending on the transition metal causing the absorption (e.g., Fe, Ti, or V) [*Wagner et al*., 1987; *Burns*, 1993b; *Cloutis et al*., 2008]. OMCT absorption features in the UV region are orders of magnitude stronger than crystal field absorptions in the 1000 nm region [*Burns*, 1993b], meaning that small amounts of Fe (or another transition metal) can cause OMCT absorptions and influence the shape of material spectra in the UV [*Rava and Hapke*, 1987; *Klima et al*., 2007, 2011; *Cloutis et al*., 2008; *Greenspon et al*., 2012]. OMCT absorptions have previously been proposed as an explanation for the shape of both disk-integrated and spatially resolved measurements of Mercury reflectance spectra acquired by the MASCS instrument [*McClintock et al*., 2008; *Holsclaw et al*., 2010].

Laboratory studies have shown that decreasing Fe content in silicate minerals and glasses will (1) weaken the strength of OMCT absorptions in the UV, (2) move the shoulder of this OMCT absorption to shorter wavelengths, and (3) increase the overall reflectance of the materials [e.g., *Rava and Hapke*, 1987; *Cloutis et al*., 2008; *Greenspon et al*., 2012]. The overall effect of these changes is that decreased Fe content will result in higher reflectance and steeper UV slopes [*Rava and Hapke*, 1987; *Cloutis et al*., 2008; *Greenspon et al*., 2012]. This trend matches the observed spectral signature of the pyroclastic deposits relative to the average spectrum for Mercury [*Izenberg et al*., 2014], and one interpretation of the MASCS data is that the pyroclastic deposits are lower in Fe than the surrounding terrain. The observed lack of a broad absorption band centered near 1000 nm in the pyroclastic deposit spectra coupled with very low global surface abundances of Fe [*Nittler et al*., 2011; *Evans et al*., 2012] limit the possibility for substantial Fe variations. The greater sensitivity of the UV region to the presence of trace amounts of iron [*Burns*, 1993b] may nonetheless permit the detection of variations in Fe abundance in the context of a broadly low-iron surface [*Nittler et al*., 2011; *Evans et al*., 2012], as has been documented from recent XRS results [*Weider et al*., 2013].

An alternative possibility is that the observed downturn in the UV region of the spectrum is due to the result of variations in the physical properties of the deposits, in particular grain size. Laboratory studies by *Cloutis et al*. [2008] have shown that, in a manner similar to the effects of increasing Fe content, increasing the grain size of silicate minerals causes OMCT bands to deepen and broaden, resulting in a shallower UV slope. This trend is observed even with spectra of a plagioclase feldspar sample that has a very low Fe concentration (0.29 wt % Fe) [*Cloutis et al*., 2008]. Additionally, a general effect of increasing grain size on spectra from the ultraviolet to the near infrared is to decrease the overall reflectance because of increased volume scattering and decreased surface reflections [e.g., *Crown and Pieters*, 1987; *Gaffey et al*., 1993; *Mustard and Hays*, 1997].

Therefore, a variation in grain size among the deposits could also explain the observed covariation of UV downturn strength and overall reflectance (Figures 11 and 12). Furthermore, because the optical properties of the finest grain-size fraction are thought to control the spectral signature of lunar soils [*Pieters et al*., 1993], variations in the amount of fine particles within the pyroclastic deposits may contribute to the observed spectral trends in the UV. If differences in grain size are responsible for the UV downturn observed in the ratioed MASCS spectra of the pyroclastic deposits, then those deposits are, on average, composed of finer-grained material than the rest of Mercury's surface [*Izenberg et al*., 2014], as is observed for the fine-grained pyroclastic material on the Moon [e.g., *Heiken et al*., 1974; *Weitz et al*., 1999].

A third possible contributor to variations in the observed UV downturn is a difference in the degree of space weathering. Space weathering on the Moon and other airless bodies is known to result in the darkening of surface material, the reduction of spectral contrast, and the reddening, or increase, of the visible to NIR spectral slope [e.g., *Hapke*, 2001; *Blewett et al*., 2009]. Much of the previous work on space weathering has focused on effects in the NIR region of the spectrum, but *Hendrix and Vilas* [2006] showed that the effect of space weathering in the UV is a decrease of the UV spectral slope. *Hendrix and Vilas* [2006] hypothesize that this change may be the result of the formation of nanophase iron coatings on mineral grains, a process also commonly invoked to explain some of the trends of space weathering in the NIR [e.g., *Pieters et al*., 1993; *Hapke*, 2001; *Noble and Pieters*, 2003]. That space weathering acts to decrease the UV spectral slope might suggest that, in the absence of other contributing factors, the pyroclastic deposits are less space weathered than Mercury's average surface [*Izenberg et al*., 2014], although the expectation that space weathering processes on Mercury operate at higher rates than on the Moon [e.g., *Cintala*, 1992; *Noble and Pieters*, 2003; *Braden and Robinson*, 2013] renders this idea unlikely.

©2014. American Geophysical Union. All Rights Reserved.

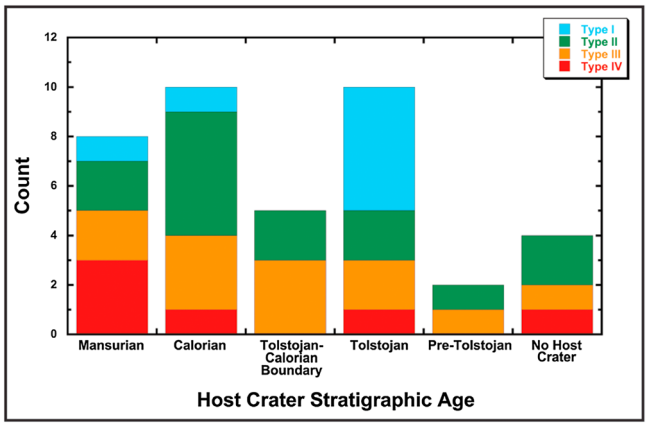


Figure 14. Stacked histogram showing the number of each MASCS type within host craters of specific stratigraphic ages. Note the fairly even distribution of MASCS types among host craters of a given stratigraphic age.

Deciding among the above three explanations for the UV downturn observed in the MASCS spectral signatures of pyroclastic deposits (Figures 10 and 11) is not possible from the observations presented here. Further analyses of MASCS data coupled with laboratory analyses of the UV–VIS spectral signatures of minerals relevant to the composition of Mercury, such as low-iron silicates, and under conditions analogous to those on Mercury's surface (e.g., with laser irradiation [*Yamada et al.*, 1999]), will illuminate more fully the origin of the spectral signatures observed for Mercury's pyroclastic deposits.

It is also worth noting that there is no obvious correlation between the spectral type of the pyroclastic deposit and the stratigraphic age of the host crater (Figure 14). Such a correlation might be expected if the spectral signature of the pyroclastic deposit material were controlled by space weathering, or even were it controlled by transition metal content if, for instance, there is a secular trend in the average composition of mantle-derived magmas with time on Mercury. The fact that the stratigraphic ages of host craters are only upper limits on the ages of the pyroclastic deposits, however, may obscure any such correlation in the data we have examined.

5.6. Spectral Variability Among Pyroclastic Deposits

Regardless of the specific source of the UV downturn in the spectral reflectance of pyroclastic deposits, this feature appears in the spectra for the majority of examined deposits and has a variable strength among deposits (Figures 10–12). This interdeposit variability allowed us to classify the pyroclastic deposits into four major categories (types I–IV) on the basis of the strength of the UV downturn parameter (Figures 11 and 12).

These four spectral types appear to make up a continuum in UV downturn strength, red spectral slope, and absolute reflectance (Figures 11 and 12). The variation in the spectral signatures of the pyroclastic deposits has two possible explanations: (1) there are variable degrees of mixing of the pyroclastic material with a spectrally distinct host rock, such as low-reflectance material or other plains material [*Robinson et al.*, 2008; *Denevi et al.*, 2009; *Izenberg et al.*, 2014] or (2) the pyroclastic deposits themselves have variable spectral signatures because of inherent differences in one or more of the factors discussed above.

Mixing with a spectrally distinct background material would be likely to result in lowering of the overall reflectance, as pyroclastic deposits are among the brightest materials on Mercury's surface [*Blewett et al.*, 2009; *Kerber et al.*, 2009, 2011; *Izenberg et al.*, 2014], as well as the subduing of spectral features [e.g., *Weitz et al.*, 1998], such as the strong UV downturn strength. Mixing with nonpyroclastic material could occur as a result of mixing with country rock in the conduit during magma ascent, mixing during ballistic emplacement of pyroclastic material on the surface [e.g., *Head and Wilson*, 1979; *Weitz et al.*, 1998; *Head et al.*, 2002] or vertical mixing and regolith development over time during impact gardening [e.g., *Oberbeck and Quaide*, 1968; *Oberbeck*, 1975].

All of these processes are likely to have occurred at the studied sites, and so different amounts of mixing with background materials is certainly a likely explanation for at least some of the interdeposit spectral variability observed (Figure 12), as has been hypothesized for interdeposit spectral variations of lunar pyroclastic deposits [e.g., *Weitz et al.*, 1998]. Further, given the spectral diversity of plains deposits across the surface of Mercury [*Robinson et al.*, 2008; *Denevi et al.*, 2009; *Izenberg et al.*, 2014], globally distributed pyroclastic deposits should also vary in their makeup, including differences in composition, physical properties such as grain size, and perhaps degree of space weathering. Although it seems likely that some combination of mixing and intrinsic differences has produced the interdeposit spectral variability observed here, determining which effects are dominant is beyond the scope of this work.

©2014. American Geophysical Union. All Rights Reserved.

6. Conclusions

We have completed an analysis of pyroclastic deposits on Mercury from imaging, spectral, and topographic data acquired during the orbital phase of the MESSENGER mission. This analysis expands the global catalog of pyroclastic deposits and brings the total number to 51. Our method for identifying new pyroclastic deposits focused on the morphological identification of candidate pyroclastic source vents. Our approach differs from that of *Kerber et al*. [2011], who searched MDIS global color mosaics for the distinctive spectral signature associated with these deposits. It is therefore likely that additional pyroclastic deposits will be discovered in the future with the use of methods complementary to those used here.

On the basis of global assessments of source vent areas and depths, deposit areas, geological associations of the deposits, relative ages of the deposits, and spectral characteristics of the deposits, the principal conclusions are as follows:

1. The great majority (~90%) of pyroclastic deposits are found within impact craters and basins. Such localization may be the result of easier access of magma to the surface because of impact-induced fracturing and reduced crustal thickness beneath the largest impact features [e.g., *Head and Wilson*, 1992].
2. Crosscutting relationships and the degradation state of the impact craters that host pyroclastic deposits suggest that explosive volcanic activity on Mercury likely occurred over a substantial fraction of Mercury's geologic history, with the emplacement of some pyroclastic deposits as recently as the Mansurian period, which ranges from ~3.25 to 1 Ga.
3. Most pyroclastic deposits are distant from smooth plains deposits, but some are located around smooth plains margins. The relation of the latter deposits to smooth plains on Mercury is similar to that seen for many lunar pyroclastic deposits adjacent to lunar maria [e.g., *Head and Wilson*, 1979; *Gaddis et al*., 1985; *Weitz et al*., 1998].
4. The spectral reflectance of pyroclastic deposits shows high overall reflectance values, a redder slope, and a downturn at UV wavelengths compared with that for surrounding material or spectrally average material on Mercury. Possible explanations include the following: (1) the deposits are poor in transition metals compared with surrounding terrain, (2) the deposits consist of finer-grained material than the surrounding terrain, or (3) the deposits are less space weathered than the surrounding terrain.
5. There is a covariation among pyroclastic deposits in the strength of the downturn in the UV and the absolute reflectance value. These interdeposit variations may be due to (1) variable amounts of mixing with underlying material [e.g., *Head and Wilson*, 1979; *Weitz et al*., 1998; *Head et al*., 2002] or (2) intrinsic chemical or physical differences (e.g., differences in grain size or mineralogy) among deposits.

Acknowledgments

We gratefully acknowledge the contributions of the engineers and managers of the MESSENGER mission that have made this work possible. The MESSENGER mission is supported by the NASA Discovery Program under contract NAS5-97271 to The Johns Hopkins University Applied Physics Laboratory and NASW-00002 to the Carnegie Institution of Washington. Sebastien Besse, Paul Byrne, Olaf Gustafson, and Catherine Weitz provided thorough and constructive reviews that improved this paper. We thank C.I. Fassett for assistance with topographic data, and J.L. Dickson and D.M.H. Baker for the help in processing image data. Thanks are also extended to D.M.H. Baker, M. Beach, D.M. Hurwitz, L.M. Jozwiak, K.E. Scanlon, W.M. Vaughan, and J.L. Whitten for assistance with the initial search for potential pyroclastic source vents and helpful discussions.

References

Adams, J. B. (1974), Visible and near-infrared diffuse reflectance spectra of pyroxenes as applied to remote sensing of solid objects in the solar system, *J. Geophys. Res.*, *79*, 4829–4836, doi:10.1029/JB079i032p04829.

Baker, D. M. H., J. W. Head, S. C. Schon, C. M. Ernst, L. M. Prockter, S. L. Murchie, B. W. Denevi, S. C. Solomon, and R. G. Strom (2011), The transition from complex crater to peak-ring basin on Mercury: New observations from MESSENGER flyby data and constraints on basin formation models, *Planet. Space Sci.*, *59*, 1932–1948, doi:10.1016/j.pss.2011.05.010.

Banks, M. E., T. R. Watters, R. G. Strom, S. C. Solomon, S. E. Braden, C. R. Chapman, Z. Xiao, and N. G. Barlow (2012), Stratigraphic relationships between lobate scarps and young impact craters on Mercury: Implications for the duration of lobate scarp formation, *Lunar Planet. Sci.*, *43*, abstract 2684.

Benz, W., W. L. Slattery, and A. G. W. Cameron (1988), Collisional stripping of Mercury's mantle, *Icarus*, *74*, 516–528.

Blewett, D. T., M. S. Robinson, B. W. Denevi, J. J. Gillis-Davis, J. W. Head, S. C. Solomon, G. M. Holsclaw, and W. E. McClintock (2009), Multispectral images of Mercury from the first MESSENGER flyby: Analysis of global and regional color trends, *Earth Planet. Sci. Lett.*, *285*, 272–282, doi:10.1016/j.epsl.2009.02.021.

Blewett, D. T., et al. (2011), Hollows on Mercury: MESSENGER evidence for geologically recent volatile-related activity, *Science*, *333*, 1856–1859, doi:10.1126/science.1211681.

Blewett, D. T., W. M. Vaughan, Z. Xiao, N. L. Chabot, B. W. Denevi, C. M. Ernst, and J. W. Head (2013), Mercury's hollows: Constraints on formation and composition from analysis of geological setting and spectral reflectance, *J. Geophys. Res. Planets*, *118*, 1013–1032, doi:10.1029/2012JE004174.

Boynton, W. V., A. L. Sprague, S. C. Solomon, R. D. Starr, L. G. Evans, W. C. Feldman, J. I. Trombka, and E. A. Rhodes (2007), MESSENGER and the chemistry of Mercury's surface, *Space Sci. Rev.*, *131*, 85–104, doi:10.1007/s11214-007-9258-3.

Braden, S. E., and M. S. Robinson (2013), Relative regolith optical maturation rates on Mercury and the Moon, *J. Geophys. Res. Planets*, *118*, 1903–1914, doi:10.1002/jgre.20143.

Burns, R. G. (1993a), *Mineralogical Applications of Crystal Field Theory*, 2nd ed., 551 pp., Cambridge Univ. Press, New York, N. Y.

Burns, R. G. (1993b), Origin of electronic spectra of minerals in the visible to near-infrared region, in *Remote Geochemical Analysis: Elemental and Mineralogical Composition*, edited by C. M. Pieters and P. A. J. Englert, pp. 3–29, Cambridge Univ. Press, Cambridge, United Kingdom.

Cameron, A. G. W. (1985), The partial volatilization of Mercury, *Icarus*, *64*, 285–294.

©2014. American Geophysical Union. All Rights Reserved.

Cavanaugh, J. F., et al. (2007), The Mercury Laser Altimeter instrument for the MESSENGER mission, *Space Sci. Rev.*, *131*, 451–479, doi:10.1007/s11214-007-9273-4.
Cintala, M. J. (1992), Impact-induced thermal effects in the lunar and mercurian regoliths, *J. Geophys. Res.*, *97*, 947–973, doi:10.1029/91JE02207.
Cloutis, E. A., K. A. McCormack, J. F. Bell, A. R. Hendrix, D. T. Bailey, M. A. Craig, S. A. Mertzman, M. S. Robinson, and M. A. Riner (2008), Ultraviolet spectral reflectance properties of common planetary minerals, *Icarus*, *197*, 321–347, doi:10.1016/j.icarus.2008.04.018.
Crown, D. A., and C. M. Pieters (1987), Spectral properties of plagioclase and pyroxene mixtures and the interpretation of lunar soil spectra, *Icarus*, *72*, 492–506.
Denevi, B. W., et al. (2009), The evolution of Mercury's crust: A global perspective from MESSENGER, *Science*, *324*, 613–618, doi:10.1126/science.1172226.
Denevi, B. W., et al. (2013), The distribution and origin of smooth plains on Mercury, *J. Geophys. Res. Planets*, *118*, 891–907, doi:10.1002/jgre.20075.
Domingue, D. L., F. Vilas, G. M. Holsclaw, J. Warell, N. R. Izenberg, S. L. Murchie, B. W. Denevi, D. T. Blewett, W. E. McClintock, and B. J. Anderson (2010), Whole-disk spectrophotometric properties of Mercury: Synthesis of MESSENGER and ground-based observations, *Icarus*, *209*, 101–124, doi:10.1016/j.icarus.2010.02.022.
Domingue, D. L., S. L. Murchie, N. L. Chabot, B. W. Denevi, and F. Vilas (2011), Mercury's spectrophotometric properties: Update from the Mercury Dual Imaging System observations during the third MESSENGER flyby, *Planet. Space Sci.*, *59*, 1853–1872, doi:10.1016/j.pss.2011.04.012.
Evans, L. G., et al. (2012), Major-element abundances on the surface of Mercury: Results from the MESSENGER Gamma-Ray Spectrometer, *J. Geophys. Res.*, *117*, E00L07, doi:10.1029/2012JE004178.
Gaddis, L. R., C. M. Pieters, and B. R. Hawke (1985), Remote sensing of lunar pyroclastic mantling deposits, *Icarus*, *61*, 461–489.
Gaffey, S. J., L. A. McFadden, D. Nash, and C. M. Pieters (1993), Ultraviolet, visible, and near-infrared reflectance spectroscopy: Laboratory spectra of geologic materials, in *Remote Geochemical Analysis: Elemental and Mineralogical Composition*, edited by C. M. Pieters and P. A. J. Englert, pp. 43–77, Cambridge Univ. Press, Cambridge, United Kingdom.
Geyer, A., and J. Martí (2008), The new worldwide collapse caldera database (CCDB): A tool for studying and understanding caldera processes, *J. Volcanol. Geotherm. Res.*, *175*, 334–354, doi:10.1016/j.jvolgeores.2008.03.017.
Gillis-Davis, J. J., D. T. Blewett, R. W. Gaskell, B. W. Denevi, M. S. Robinson, R. G. Strom, S. C. Solomon, and A. L. Sprague (2009), Pit-floor craters on Mercury: Evidence of near-surface igneous activity, *Earth Planet. Sci. Lett.*, *285*, 243–250, doi:10.1016/j.epsl.2009.05.023.
Greenspon, A. S., C. A. Hibbitts, and M. D. Dyar (2012), Compositional dependencies in ultraviolet reflectance spectra of synthetic glasses relevant to airless bodies, *Lunar Planet. Sci.*, *43*, abstract 2490.
Gwinner, K., J. W. Head, J. Oberst, J. J. Gillis-Davis, Z. Xiao, R. G. Strom, F. Preusker, and S. C. Solomon (2012), Morphology of pit craters on Mercury from stereo-derived topography and implications for pit crater formation, *Lunar Planet. Sci.*, *43*, abstract 1991.
Hapke, B. (2001), Space weathering from Mercury to the asteroid belt, *J. Geophys. Res.*, *106*, 10,039–10,073.
Hartmann, W. K. (1966), Martian cratering, *Icarus*, *5*, 565–576.
Hartmann, W. K. (1977), Relative crater production rates on planets, *Icarus*, *31*, 260–276.
Hauck, S. A., II, A. J. Dombard, R. J. Phillips, and S. C. Solomon (2004), Internal and tectonic evolution of Mercury, *Earth Planet. Sci. Lett.*, *222*, 713–728, doi:10.1016/j.epsl.2004.03.037.
Hawkins, S. E. III, et al. (2007), The Mercury Dual Imaging System on the MESSENGER spacecraft, *Space Sci. Rev.*, *131*, 247–338, doi:10.1007/s11214-007-9266-3.
Head, J. W., and L. Wilson (1979), Alphonsus-type dark-halo craters: Morphology, morphometry and eruption conditions, in *Proc. Lunar Planet. Sci. Conf., 10th*, vol. 3, pp. 2861–2897, Pergamon Press, New York.
Head, J. W., and L. Wilson (1992), Lunar mare volcanism: Stratigraphy, eruption conditions, and the evolution of secondary crusts, *Geochim. Cosmochim. Acta*, *56*, 2155–2175.
Head, J. W., L. Wilson, and C. M. Weitz (2002), Dark ring in southwestern Orientale basin: Origin as a single pyroclastic eruption, *J. Geophys. Res.*, *107* (E1), 5001, doi:10.1029/2000JE001438.
Head, J. W., C. R. Chapman, D. L. Domingue, S. E. Hawkins, W. E. McClintock, S. L. Murchie, L. M. Prockter, M. S. Robinson, R. G. Strom, and T. R. Watters (2007), The geology of Mercury: The view prior to the MESSENGER mission, *Space Sci. Rev.*, *131*, 41–84, doi:10.1007/s11214-007-9263-6.
Head, J. W., et al. (2008), Volcanism on Mercury: Evidence from the first MESSENGER flyby, *Science*, *321*, 69–72, doi:10.1126/science.1159256.
Head, J. W., et al. (2009), Volcanism on Mercury: Evidence from the first MESSENGER flyby for extrusive and explosive activity and the volcanic origin of plains, *Earth Planet. Sci. Lett.*, *285*, 227–242, doi:10.1016/j.epsl.2009.03.007.
Head, J. W., et al. (2011), Flood volcanism in the northern high latitudes of Mercury revealed by MESSENGER, *Science*, *333*, 1853–1856, doi:10.1126/science.1211997.
Heiken, G. H., D. S. McKay, and R. W. Brown (1974), Lunar deposits of possible pyroclastic origin, *Geochim. Cosmochim. Acta*, *38*, 1703–1718.
Hendrix, A. R., and F. Vilas (2006), The effects of space weathering at UV wavelengths: S-class asteroids, *Astron. J.*, *132*, 1396–1404, doi:10.1086/506426.
Holsclaw, G. M., W. E. McClintock, D. L. Domingue, N. R. Izenberg, D. T. Blewett, and A. L. Sprague (2010), A comparison of the ultraviolet to near-infrared spectral properties of Mercury and the Moon as observed by MESSENGER, *Icarus*, *209*, 179–194, doi:10.1016/j.icarus.2010.05.001.
Izenberg, N. R., et al. (2014), The low-iron, reduced surface of Mercury as seen in spectral reflectance by MESSENGER, *Icarus*, *228*, 364–374, doi:10.1016/j.icarus.2013.10.023.
Jozwiak, L. M., and J. W. Head (2012), Mercury pit-floor craters: Perspectives on their origin from lunar floor-fractured craters, *Lunar Planet. Sci.*, *43*, abstract 2424.
Kerber, L., J. W. Head, S. C. Solomon, S. L. Murchie, D. T. Blewett, and L. Wilson (2009), Explosive volcanic eruptions on Mercury: Eruption conditions, magma volatile content, and implications for interior volatile abundances, *Earth Planet. Sci. Lett.*, *285*, 263–271, doi:10.1016/j.epsl.2009.04.037.
Kerber, L., J. W. Head, D. T. Blewett, S. C. Solomon, L. Wilson, S. L. Murchie, M. S. Robinson, B. W. Denevi, and D. L. Domingue (2011), The global distribution of pyroclastic deposits on Mercury: The view from MESSENGER flybys 1–3, *Planet. Space Sci.*, *59*, 1895–1909, doi:10.1016/j.pss.2011.03.020.
King, T. V. V., and W. I. Ridley (1987), Relation of the spectroscopic reflectance of olivine to mineral chemistry and some remote sensing implications, *J. Geophys. Res.*, *92*, 11,457–11,469, doi:10.1029/JB092iB11p11457.
Klima, R. L., C. M. Pieters, and M. D. Dyar (2007), Spectroscopy of synthetic Mg-Fe pyroxenes I: Spin-allowed and spin-forbidden crystal field bands in the visible and near-infrared, *Meteorit. Planet. Sci.*, *42*, 235–253, doi:10.1111/j.1945-5100.2007.tb00230.x.
Klima, R. L., M. D. Dyar, and C. M. Pieters (2011), Near-infrared spectra of clinopyroxenes: Effects of calcium content and crystal structure, *Meteorit. Planet. Sci.*, *46*, 379–395, doi:10.1111/j.1945-5100.2010.01158.x.
Lipman, P. W. (1997), Subsidence of ash-flow calderas: Relation to caldera size and magma-chamber geometry, *Bull. Volcanol.*, *59*, 198–218, doi:10.1007/s004450050186.

©2014. American Geophysical Union. All Rights Reserved.

Lucchitta, B. K., and H. H. Schmitt (1974), Orange material in the Sulpicius Gallus Formation at the southwestern edge of Mare Serenitatis, in *Proc. Lunar Sci. Conf., 5th*, vol. 1, pp. 223–234, Pergamon Press, New York.
Mazarico, E., D. D. Rowlands, G. A. Neumann, D. E. Smith, M. H. Torrence, F. G. Lemoine, and M. T. Zuber (2012), Orbit determination of the Lunar Reconnaissance Orbiter, *J. Geod.*, *86*, 193–207, doi:10.1007/s00190-011-0509-4.
McClintock, W. E., and M. R. Lankton (2007), The Mercury Atmospheric and Surface Composition Spectrometer for the MESSENGER mission, *Space Sci. Rev.*, *131*, 481–521, doi:10.1007/s11214-007-9264-5.
McClintock, W. E., et al. (2008), Spectroscopic observations of Mercury's surface reflectance during MESSENGER's first Mercury flyby, *Science*, *321*, 62–65, doi:10.1126/science.1159933.
McCord, T. B., M. P. Charette, T. V. Johnson, L. A. Lebofsky, C. Pieters, and J. B. Adams (1972), Lunar spectral types, *J. Geophys. Res.*, *77*, 1349–1359.
McCord, T. B., R. N. Clark, B. R. Hawke, L. A. McFadden, and P. D. Owensby (1981), Moon: Near-infrared spectral reflectance, a first good look, *J. Geophys. Res.*, *86*, 10,883–10,892.
Murchie, S. L., et al. (2008), Geology of the Caloris basin, Mercury: A view from MESSENGER, *Science*, *321*, 73–76, doi:10.1126/science.1159261.
Mustard, J. F., and J. E. Hays (1997), Effects of hyperfine particles on reflectance spectra from 0.3 to 25 μm, *Icarus*, *125*, 145–163.
Neukum, G., B. König, H. Fechtig, and D. Storzer (1975), Cratering in the Earth-Moon system: Consequences for age determination by crater counting, in *Proc. Lunar Sci. Conf., 6th*, vol. 3, pp. 2597–2620, Pergamon Press, New York.
Nittler, L. R., et al. (2011), The major-element composition of Mercury's surface from MESSENGER X-ray spectrometry, *Science*, *333*, 1847–1850, doi:10.1126/science.1211567.
Noble, S. K., and C. M. Pieters (2003), Space weathering on Mercury: Implications for remote sensing, *Solar System Res.*, *37*, 31–35.
Oberbeck, V. R. (1975), The role of ballistic erosion and sedimentation in lunar stratigraphy, *Rev. Geophys. Space Phys.*, *13*, 337–362.
Oberbeck, V. R., and W. L. Quaide (1968), Genetic implications of lunar regolith thickness variations, *Icarus*, *9*, 446–465.
Pashai, P., N. R. Izenberg, J. J. Gillis-Davis, T. R. Watters, D. T. Blewett, and S. C. Solomon (2010), A Mercury impact crater with volcanic and tectonic modification, *Lunar Planet. Sci.*, *41*, abstract 1693.
Pieters, C. M., E. M. Fischer, O. Rode, and A. Basu (1993), Optical effects of space weathering: The role of the finest fraction, *J. Geophys. Res.*, *98*, 20,817–20,824.
Prockter, L. M., et al. (2010), Evidence for young volcanism on Mercury from the third MESSENGER flyby, *Science*, *329*, 668–671, doi:10.1126/science.1188186.
Prockter, L. M., S. L. Murchie, C. M. Ernst, D. M. H. Baker, P. K. Byrne, J. W. Head, T. R. Watters, B. W. Denevi, C. R. Chapman, and S. C. Solomon (2012), The geology of medium-sized basins on Mercury: Implications for surface processes and evolution, *Lunar Planet. Sci.*, *43*, abstract 1326.
Rava, B., and B. Hapke (1987), An analysis of the Mariner 10 color ratio map of Mercury, *Icarus*, *71*, 397–429.
Robinson, M. S., and P. G. Lucey (1997), Recalibrated Mariner 10 color mosaics: Implications for Mercurian volcanism, *Science*, *275*, 197–200, doi:10.1126/science.275.5297.197.
Robinson, M. S., et al. (2008), Reflectance and color variations on Mercury: Regolith processes and compositional heterogeneity, *Science*, *321*, 66–69, doi:10.1126/science.1160080.
Robinson, M. S., et al. (2010), Lunar Reconnaissance Orbiter Camera (LROC) instrument overview, *Space Sci. Rev.*, *150*, 81–124, doi:10.1007/s11214-010-9634-2.
Smith, D. E., et al. (2010), The Lunar Orbiter Laser Altimeter investigation on the Lunar Reconnaissance Orbiter mission, *Space Sci. Rev.*, *150*, 209–241, doi:10.1007/s11214-009-9512-y.
Solomon, S. C., R. L. McNutt Jr., R. E. Gold, and D. L. Domingue (2007), MESSENGER mission overview, *Space Sci. Rev.*, *131*, 3–39, doi:10.1007/s11214-007-9247-6.
Solomon, S. C., et al. (2008), Return to Mercury: A global perspective on MESSENGER's first Mercury flyby, *Science*, *321*, 59–62, doi:10.1126/science.1159706.
Spudis, P. D., and J. E. Guest (1988), Stratigraphy and geologic history of Mercury, in *Mercury*, edited by F. Vilas, C. R. Chapman, and M. S. Matthews, pp. 118–164, University of Arizona Press, Tuscon, Ariz.
Strom, R. G., N. J. Trask, and J. E. Guest (1975), Tectonism and volcanism on Mercury, *J. Geophys. Res.*, *80*, 2478–2507, doi:10.1029/JB080i017p02478.
Thomas, R. J., D. A. Rothery, S. J. Conway, and M. Anand (2014), Hollows on Mercury: Materials and mechanisms involved in their formation, *Icarus*, *229*, 221–235, doi:10.1016/j.icarus.2013.11.018.
Vaughan, W. M., J. Helbert, D. T. Blewett, J. W. Head, S. L. Murchie, K. Gwinner, T. J. McCoy, and S. C. Solomon (2012), Hollow-forming layers in impact craters on Mercury: Massive sulfide or chloride deposits formed by impact melt differentiation?, *Lunar Planet. Sci.*, *43*, abstract 1187.
Wagner, J. K., B. W. Hapke, and E. N. Wells (1987), Atlas of reflectance spectra of terrestrial, lunar, and meteoritic powders and frosts from 92 to 1800 nm, *Icarus*, *69*, 14–28.
Watters, T. R., M. S. Robinson, and A. C. Cook (1998), Topography of lobate scarps on Mercury: New constraints on the planet's contraction, *Geology*, *26*, 991–994.
Watters, T. R., J. W. Head, S. C. Solomon, M. S. Robinson, C. R. Chapman, B. W. Denevi, C. I. Fassett, S. L. Murchie, and R. G. Strom (2009), Evolution of the Rembrandt impact basin on Mercury, *Science*, *324*, 618–621, doi:10.1126/science.1172109.
Weider, S. Z., L. R. Nittler, R. D. Starr, and S. C. Solomon (2013), The distribution of iron on the surface of Mercury from MESSENGER X-Ray Spectrometer measurements, *Lunar Planet. Sci.*, *44*, abstract 2189.
Weitz, C. M., J. W. Head, and C. M. Pieters (1998), Lunar regional dark mantle deposits: Geologic, multispectral, and modeling studies, *J. Geophys. Res.*, *103*, 22,725–22,759.
Weitz, C. M., M. J. Rutherford, J. W. Head, and D. S. McKay (1999), Ascent and eruption of a lunar high-titanium magma as inferred from the petrology of the 74001/2 drill core, *Meteorit. Planet. Sci.*, *34*, 527–540, doi:10.1111/j.1945-5100.1999.tb01361.x.
Wilson, L., and J. W. Head (2008), Volcanism on Mercury: A new model for the history of magma ascent and eruption, *Geophys. Res. Lett.*, *35*, L23205, doi:10.1029/2008GL035620.
Wilson, L., and J. W. Head (2012), Volcanic eruption processes on Mercury, *Lunar Planet. Sci.*, *43*, abstract 1316.
Yamada, M., S. Sasaki, H. Nagahara, A. Fujiwara, S. Hasegawa, H. Yano, T. Hiroi, H. Ohashi, and H. Otake (1999), Simulation of space weathering of planet-forming minerals: Nanosecond pulse laser irradiation and proton implantation on olivine and pyroxene samples, *Earth Planets Space*, *51*, 1255–1265.
Zolotov, M. Y. (2011), On the chemistry of mantle and magmatic volatiles on Mercury, *Icarus*, *212*, 24–41, doi:10.1016/j.icarus.2010.12.014.
Zuber, M. T., et al. (2012), Topography of the northern hemisphere of Mercury from MESSENGER laser altimetry, *Science*, *336*, 217–220, doi:10.1126/science.1218805.

©2014. American Geophysical Union. All Rights Reserved.